

**UNCLASSIFIED**

**SPEC**<sub>inc</sub>



**“Characterization of Aerosol Inlets and Ducts”  
Topic No. N01-047  
Draft Final Report**

**R. Paul Lawson, Principal Investigator**

**SPEC, Inc.  
3022 Sterling Circle, Suite 200  
Boulder, CO 80301**

**Contract No. N00014-01-M-0122  
Office of Naval Research**

**For the Period 1 May 2001 – 30 September 2001**

**NOTE: Approved for public release; SBIR report, distribution unlimited.**

**UNCLASSIFIED**

**20011005 367**

REPORT DOCUMENTATION PAGE				Form Approved OMB No. 0704-0188	
<small>Public reporting burden for this collection of information is estimated to average 1 hour per response, including the time for reviewing instructions, searching data sources, gathering and maintaining the data needed, and completing and reviewing the collection of information. Send comments regarding this burden estimate or any other aspect of this collection of information, including suggestions for reducing this burden to Washington Headquarters Service, Directorate for Information Operations and Reports, 1215 Jefferson Davis Highway, Suite 1204, Arlington, VA 22202-4302, and to the Office of Management and Budget, Paperwork Reduction Project (0704-0188) Washington, DC 20503.</small> <b>PLEASE DO NOT RETURN YOUR FORM TO THE ABOVE ADDRESS.</b>					
1. REPORT DATE (DD-MM-YYYY)		2. REPORT DATE TYPE		3. DATES COVERED (From - To)	
October 2, 2001		Draft Final Progress Report		1 May - 30 September 2001	
4. TITLE AND SUBTITLE  "Characterization of Aerosol Inlets and Ducts"				5a. CONTRACT NUMBER	
				N00014-01-M-0122	
				5b. GRANT NUMBER	
				N/A	
				5c. PROGRAM ELEMENT NUMBER	
				N/A	
6. AUTHOR(S)  Patrick Zmarzly, R. Paul Lawson				5d. PROJECT NUMBER	
				N/A	
				5e. TASK NUMBER	
				N/A	
				5f. WORK UNIT NUMBER	
				N/A	
7. PERFORMING ORGANIZATION NAME(S) AND ADDRESS(ES)				8. PERFORMING ORGANIZATION REPORT NUMBER	
SPEC, Inc. 3022 Sterling Circle, Suite 200 Boulder, CO 80301				Draft Final Progress Report	
9. SPONSORING/MONITORING AGENCY NAME(S) AND ADDRESS(ES)  Office of Naval Research ONR 253 JROFRANO Ballston Tower One 800 North Quincy St., Arlington, VA 22217-5660				10. SPONSOR/MONITOR'S ACRONYM(S)	
				ONR	
				11. SPONSORING/MONITORING AGENCY REPORT NUMBER	
				N/A	
12. DISTRIBUTION AVAILABILITY STATEMENT  Approved for Public Release; SBIR Report, Distribution Unlimited.					
13. SUPPLEMENTARY NOTES					
14. ABSTRACT All of the Phase I research objectives have been completed for the design, manufacture, and testing of the aerosol inlet calibration device. Optical simulations have been performed that indicate the presence of the inlet calibration device will have minimal effect on measurements from the FSSP 100. The mechanical design, manufacture, and assembly of the inlet calibration device were successfully completed. The inlet calibration device has been successfully tested in the laboratory with an FSSP 100. The measurements from the FSSP 100 with and without the inlet calibration device were nearly identical for Operating Ranges 1 and 2. The laboratory results confirm that the effect of the inlet calibration device on the measurements is negligible. At this time, SPEC recommends proceeding to Phase II, based on the results of the Phase I effort.					
15. SUBJECT TERMS					
16. SECURITY CLASSIFICATION OF:			17. LIMITATION OF ABSTRACT	18. NUMBER OF PAGES	19a. NAME OF RESPONSIBLE PERSON
a. REPORT	b. ABSTRACT	c. THIS PAGE			Paul Lawson, Principal Invest.
				40(incl SF298)	19b. TELEPHONE NUMBER (Include area code) (303) 449-1105

# 1. Identification and Significance of the Problem

Consideration of the effects of aerosol particles on climate is not new and some studies date back more than seventy years (e.g., Ångström 1929). Hobbs et al. (1974) and Mitchell (1975) discuss the effects of the production of sulfate aerosols and greenhouse gases from the burning of fossil fuels. Unfortunately, the international monitoring programs that were established in the 1960s and 1970s failed to produce a usable database due to inadequate instrumentation and lack of continuity in the observations (Charlson et al. 1991). The predicted effects of sulfate aerosol on the earth's radiation budget and global climate change have since received much attention in the literature (e.g., Charlson et al. 1987; Wigley 1989, 1991; Charlson et al. 1990, 1991; 1992; Hegg et al. 1991; Boucher and Anderson 1995; Nemessure et al. 1995).

Charlson et al. (1992) pointed out that, contrary to previous thought, anthropogenic aerosols, which are mainly composed of sulfates, contribute substantially to radiative forcing and may have a significant impact on climate forcing. There are three principal mechanisms whereby particulate sulfates affect the earth's radiation budget:

- i. Biogenic sulfur gas emissions from the oceans convert to sulfates which can become cloud condensation nuclei (CCN) that modulate the albedo of maritime stratus clouds (Charlson et al. 1987).
- ii. Anthropogenic production of sulfates may raise the CCN concentration and modulate the cloud albedo (Wigley 1989; Twomey et al. 1984).
- iii. The albedo of sulfate aerosol itself is relatively high and anthropogenic production of sulfates could have a significant effect on the earth's albedo (Charlson et al. 1990, 1991; 1992; Wigley 1991).

The first two mechanisms have an *indirect* effect on the radiative budget by altering the cloud condensation nucleus (CCN) spectrum, which can modify the short wave reflective properties of clouds. The third mechanism has a *direct* effect on the radiative forcing. The results of Charlson et al. (1992) show that the net effect of both the *direct* and *indirect* contributions work to increase planetary albedo, thereby producing a cooling effect on the order of  $1 \text{ W m}^{-2}$ , which is comparable in magnitude but opposite in sign to current anthropogenic greenhouse gas forcing.

Sulfates generated from burning of fossil fuels are the major constituent of anthropogenic aerosols, of which the large majority are  $< 1 \mu\text{m}$  in size (Charlson et al. 1974; Tanner et al. 1977). However, larger aerosols generated by erosion processes (i.e., wind-blown mineral dust, tire erosion, etc.) are also thought to have significant impacts on climate forcing. Wind-blown mineral dust, which is typically composed of  $\text{K}^+$ ,  $\text{Na}^+$ ,  $\text{Mg}^+$  and  $\text{Ca}^{++}$ , comprises about 50% of total atmospheric dust. Tegen et al. (1996) show that the radiative forcing of dust can be either positive or negative, depending on clear/cloudy sky conditions and surface albedo. Optical effects of aerosols have been shown to depend largely on size and composition (e.g., Boucher and Anderson 1995; Nemessure et al. 1995; Tegen et al. 1996). Thus, both aerosol

composition and size distribution are significant factors that need to be quantified in order to determine the net radiative properties of aerosols.

The effect that aerosols have on clouds and precipitation could play an even larger role in both the planetary radiative and hydrological cycles. Albrecht (1989) has suggested that the drizzle, which normally occurs in marine stratocumulus clouds in clean air, would be inhibited from (polluted) clouds with a smaller droplet size. Recently, Rosenfeld (1999) used measurements from the TRMM satellite to show that smoke from burning vegetation suppresses precipitation, and Rosenfeld (2000) used TRMM data to show that precipitation was suppressed downwind of urban and industrial air pollution. Even larger aerosols may play a role in facilitating precipitation in warm cumulus clouds. Laird et al. (2000) show aircraft measurements suggesting that "ultrafine nuclei", wetted aerosols with diameters from about 20 to 300  $\mu\text{m}$ , accelerate the coalescence process and rainfall in warm Florida cumuli.

From the foregoing discussion, it is apparent that aerosol size and composition play an important role in both direct and indirect radiative forcing, as well as the development of clouds and precipitation. The size and concentration measurements of aerosols with diameters from about 0.5 to 50  $\mu\text{m}$  can be accomplished using optical particle samplers installed on research aircraft (e.g., Baumgardner et al. 1992). However, smaller particles and aerosol composition are best measured by first bringing outside air into the cabin of an aircraft, decelerating the flow, and then injecting the air sample into instruments that typically require a few or several seconds to perform analyses.

Several studies have shown that significant losses occur in aerosol inlets and tubing when the airflow is decelerated, typically from an aircraft velocity of about 100  $\text{m s}^{-1}$  to a few  $\text{m s}^{-1}$ , so aerosols can be ingested into counters and spectrometers in the cabin (e.g. Huebert et al. 1990, 2000; Baumgardner et al. 1991; Porter et al. 1992; Sheridan and Norton 1998). These studies have shown that the most significant losses in decelerating diffusers occur for particles larger than about 1  $\mu\text{m}$  in diameter, due to highly turbulent flow just inside the tip that causes the larger particles to be impacted on the walls of the diffuser. The NCAR Community Aerosol Inlet (CAI) was developed in an effort to improve upon the performance of decelerating diffuser (DD) inlets. Blomquist et al. (2000), reporting on the Community Aerosol Inlet Evaluation Experiment (CAINE-2), found that the CAI worked well for submicron particles, but its efficiency dropped rapidly for larger particles, with a 50% cut size in the 2-3  $\mu\text{m}$  range. Huebert et al. (2000) report on the performance of the CAI, a shrouded solid-diffuser/curved-tube inlet (SD) developed by NASA, and a new low turbulence inlet (LTI) developed at the University of Denver (Seebaugh et al. 1997). The inlet that performed the best in this intercomparison was the LTI, which uses suction to control the boundary layer inside the inlet. The LTI passed about twice as many supermicron particles as the SD, and up to ten times as many of the larger particles as the CAI.

Huebert et al. (2000) attempted to quantify the losses in aerosol inlets and tubing by comparing FSSP-300 aerosol size distributions measured on the wing of the C-130 and at the outlets of the tubing in the cabin. They concluded that the FSSP-300 measurements in the cabin were inconsistent and unusable. Although they could not be certain of the reason for the unreliability of the FSSP-300 measurements in the cabin, they suggested that the calibration device introduced errors by creating a "jet

flow" through the sample volume. The calibration device is basically a plug that is inserted into the 1.5 inch diameter sample tube with a small tube in the middle that terminates just forward of the viewing area of the probe. The air and aerosol particles are accelerated in the small tube and a "jet" of air is sent through the viewing area. However, simple theory of jet flow shows that the airflow near the exit region of the nozzle undergoes drastic changes before it transitions into a self-preserving pattern.

**Figure 1** shows a textbook drawing of a typical cross-section of the flow from a plane turbulent jet (Tennekes and Lumley 1972). As can be seen in the figure, a sharp gradient of particle concentration exists across the boundaries of the mixing layers that extend downstream from the nozzle. Plane jets become self-preserving about five diameters downstream and axisymmetric jets about eight diameters downstream of the orifice (Tennekes and Lumley 1972). However, even in the self-preserving region intermittency still exists near the edges, where there are sharp gradients in particle concentration. Turbulence quantities are still evolving beyond 40 diameters downstream (Tennekes and Lumley 1972). Of course, measurements of particle concentration within the jet are predicted to change with changing air velocity and ambient air pressure. Data from the C-130 flight tests support the theoretical arguments. Huebert et al. (2000) found that the ratio of wing/cabin particle size distributions were strongly impacted by flow rate through the cabin instrument.

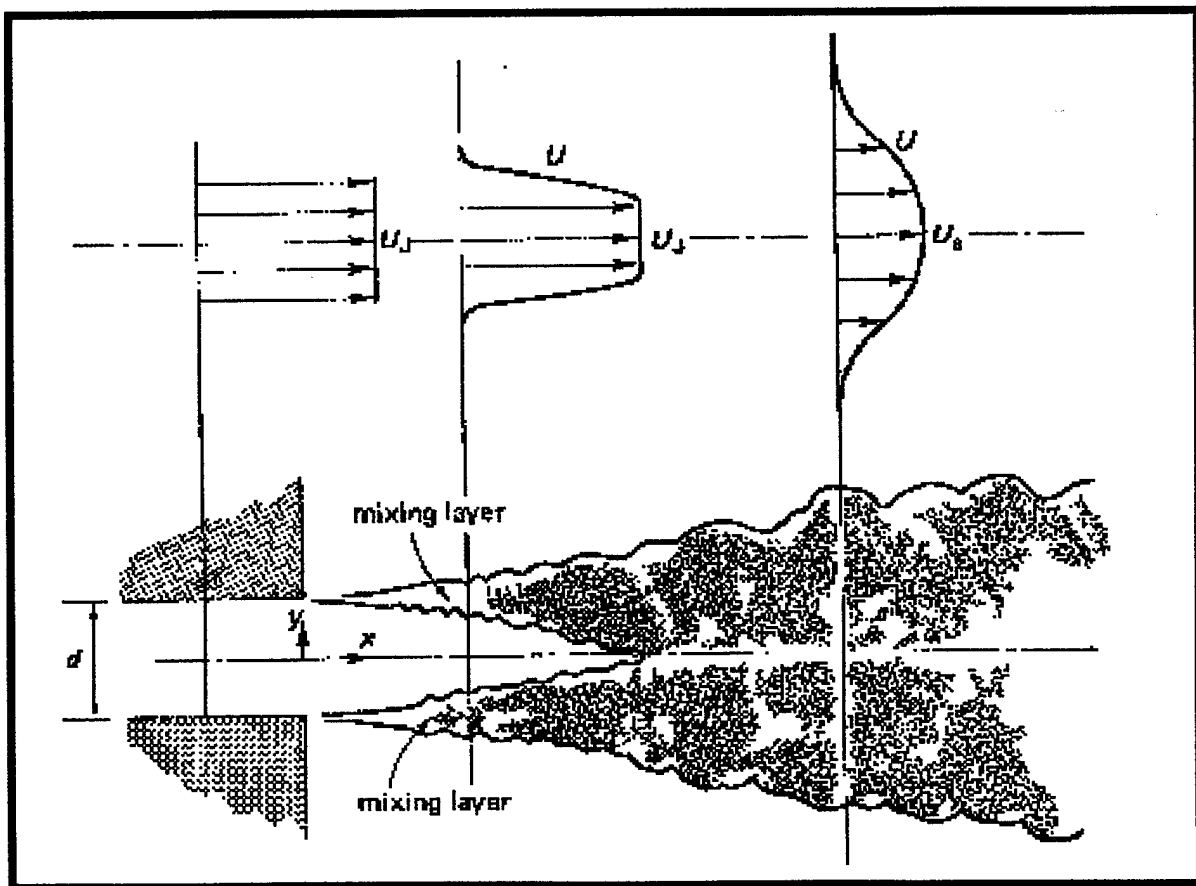


**Figure 1.** Schematic diagram showing a plane jet evolving downstream from a nozzle, such as the exit tube of the PMS FSSP insert, and (top) corresponding velocity profile.

## 2. Phase I and Phase I – II Transition Technical Objectives

### 2.1 Phase I Technical Objectives

*Following are the Technical Objectives of the Phase I research as shown in the Phase I proposal.*

The overall objective of the Phase I research will be to design, build and test in the laboratory a prototype of an aerosol inlet calibration device. The specific objectives to be met in accomplishing this goal are:

- i.* Using Zemax™ ray-tracing software, perform simulations of the optics from the FSSP-100/300 and the inlet calibration device to eliminate or minimize any optical effects from introduction of sampling windows.
- ii.* Using Solidworks™ software, design the prototype to be tested in the laboratory.
- iii.* Build the prototype.
- iv.* Test the prototype in the laboratory for effects of optical interference by making FSSP-300 measurements of the size distribution of mono-dispersed glass beads with and without the inlet calibration device.
- v.* Evaluate results from the laboratory tests, write the Phase I final report and the Phase II proposal.

## 3. Phase I Work Completed

*The following section is taken from the Phase I proposal and is included here to give the reader an overall description of the inlet calibration device. The solid model drawings of the inlet calibration device in this section were developed before the detailed mechanical design of the device occurred. Therefore, the as built inlet calibration device differs slightly from the one represented in the drawings.*

### 3.1 Description of the Inlet Calibration Device

Figures 2 - 5 show preliminary Solidworks™ drawings of the inlet calibration device. These figures are used as a reference in the following discussion. As shown in **Figure 2**, a cylindrical insert connects to the conductive tubing and slides into the sample tube of an FSSP. The orientation of the insert is fixed by the existing FSSP "scarf" tube that shields the collecting lens from water in airborne applications (**Figure 3**). The scarf tube in the FSSP-300 is the same outside diameter as in the FSSP-100. Therefore, the

inlet calibration device will be usable in both the FSSP-300 and FSSP-100, so that the size of aerosol particles can be measured out to 45  $\mu\text{m}$ , the limit of the FSSP-100.

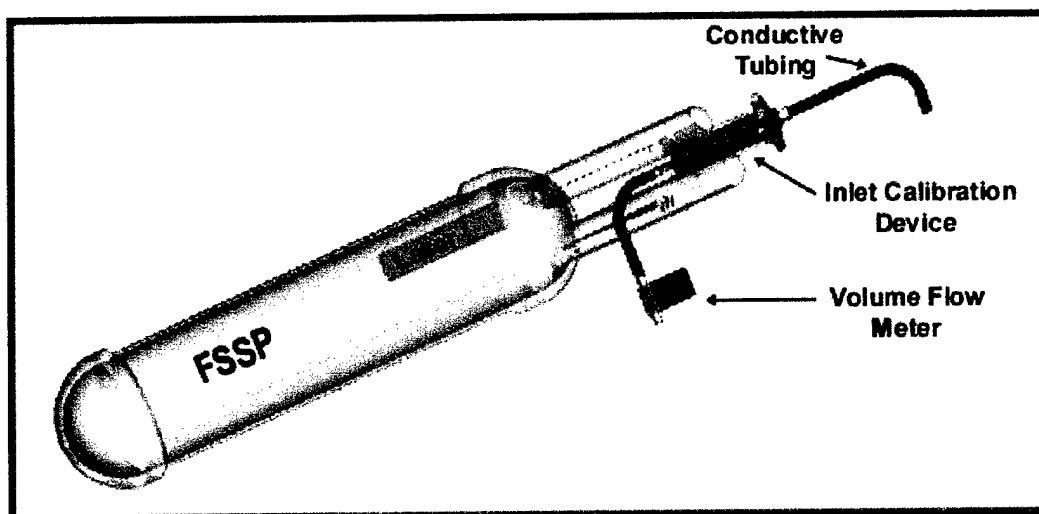


**Figure 2.** Solidworks™ CAD drawing of the inlet calibration device installed in an FSSP.

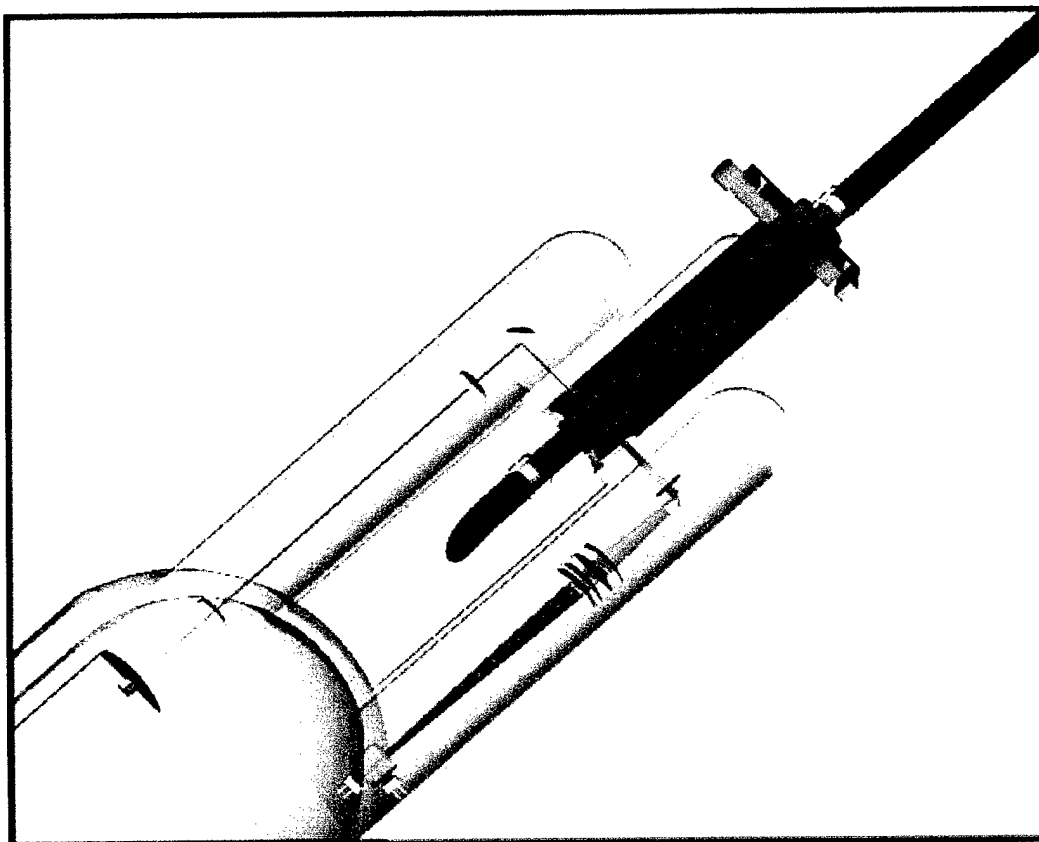


**Figure 3.** View of Inlet calibration device showing FSSP laser beam shining through optical flats inserted into the inner tube.

As shown in **Figures 3 and 5**, the transition from the inlet tube to the insert is made with a custom connector that matches the inside diameter of the tubing and the insert, so there is no distortion to the airflow at the junction. As shown in **Figures 4 and 5**, ultra thin optical flats are fused into the aluminum insert at the locations where the FSSP laser crosses the sample volume. The flow distortion at the location of the optical flats is therefore negligible. **Figure 5** also shows the precision translator that is incorporated into the insert so that the sample tube can be moved back and forth within the FSSP sample tube. In effect, translating the inlet tube across the FSSP sample tube is the same as moving the viewing area of the FSSP across the sample tube, so that a profile of particle size distributions can be made. A commercial airflow meter is attached to the exit end of the insert, so that the total airflow through the tube is recorded. The velocity distribution within a pipe is well known (see Tennekes and Lumley 1972) for the (300 to 3,000) range of Reynolds numbers found in the inlet tubes typically used for aerosol measurements. An absolute aerosol size distribution can therefore be computed by combining the total volumetric airflow with the aerosol size distribution and velocity profiles across the tube.

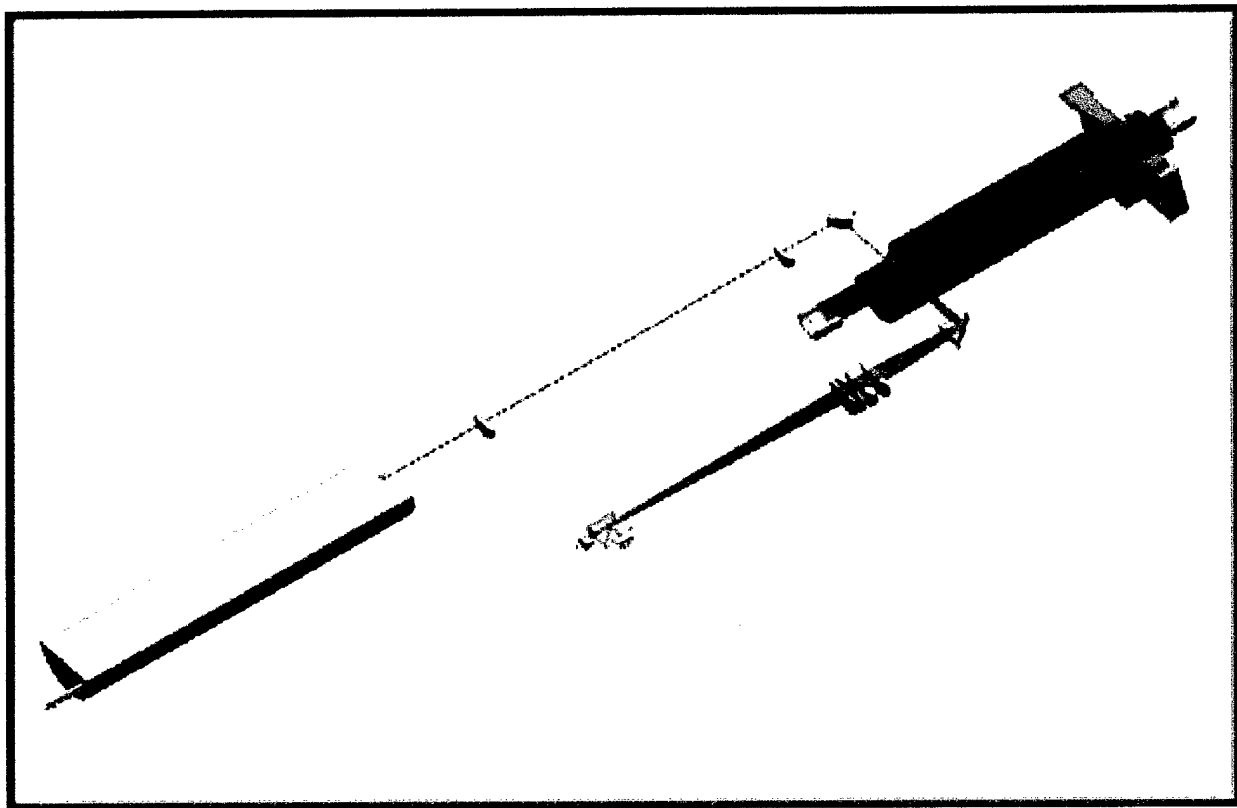


**Figure 4.** Cutaway view of the FSSP optical path and the inlet calibration device.



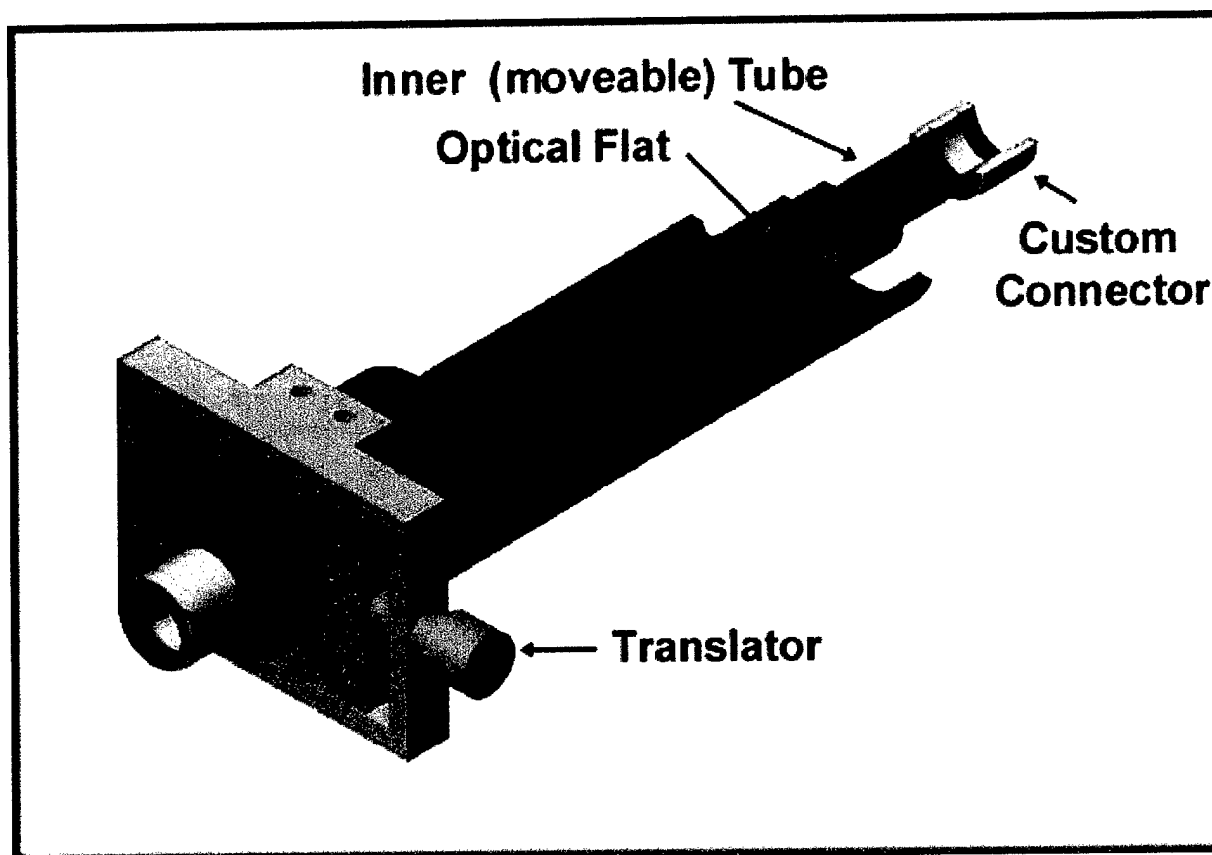


**Figure 5.** Detailed view of the insert calibration device and position translator.

Conductive tubing offered by TSI is the most commonly used tubing to connect airborne inlets to user instrumentation. The carbon-impregnated silicone tubing minimizes static charge buildup and is available with inside diameters (IDs) of 0.19" (4.8 mm), 0.31" (7.9 mm), 0.44" (11 mm) and 0.687" (17.5 mm). The prototype inlet calibration device will be fabricated in Phase I for use with an inlet tube with a 11 mm ID. This is probably the most commonly used tubing size and is mid-range in the product line. However, as a commercial product, calibration devices would be available for all four tubing IDs. To characterize the aerosol size distribution going into a user's instrument, the user would simply disconnect the inlet tube, insert it into the inlet calibration device, which has been inserted into an FSSP, and connect the output of the calibrator back into the user instrument. The aerosol size distribution would be computed and displayed in real time using a laptop computer or the existing airborne data acquisition system. This arrangement is shown conceptually in **Figure 6**, which is based on the interior of the ONR Twin Otter research aircraft. The FSSP is mounted to quick disconnects installed on each instrument rack, so that it can be readily moved from one station to another, or removed entirely when not needed for inlet calibration. The vertical orientation of the FSSP minimizes gravitational settling of larger particles into the walls of the tubing and calibration insert.

### 3.2 Ray-Tracing Optical Simulations

The optical system for the FSSP 100 was modeled using the Zemax™ optical design program. The purpose of modeling the optical system was to determine the effect of inserting sapphire windows into the FSSP optical train. For a first order approximation, the previous report indicated a longitudinal shift in the sample volume of approximately 0.217 mm away from the center of the sample tube, toward the laser side of the probe. A ray tracing analysis was performed to determine how the scattered light collection angles change with a sapphire window inserted into the optical path.

**Figure 7** is a block diagram of the optical system in the FSSP 100 taken from the FSSP 100 users manual (Baumgardner and Skinner 1989). The diagram shows the laser side and collection side of the FSSP optical system. In the absence of particles in the beam, the laser beam hits the dump spot to prevent saturation of the detectors. As particles move through the sample tube, they intersect the laser beam in the particle plane (sample volume) and scatter light around the dump spot. A 90-degree prism then folds the scattered light. Downstream of the prism, the objective lens collects the scattered light and focuses it onto the photodetector module. The module contains two detectors, the masked aperture photodiode and the signal photodiode. The combination of these detectors is used to determine if the particle is within the depth of field. The intensity on the signal detector alone is used to size the particles. The analysis here deals with the collection side of the optical system and how changing the collection angles will affect the light intensity on the signal photodetector.

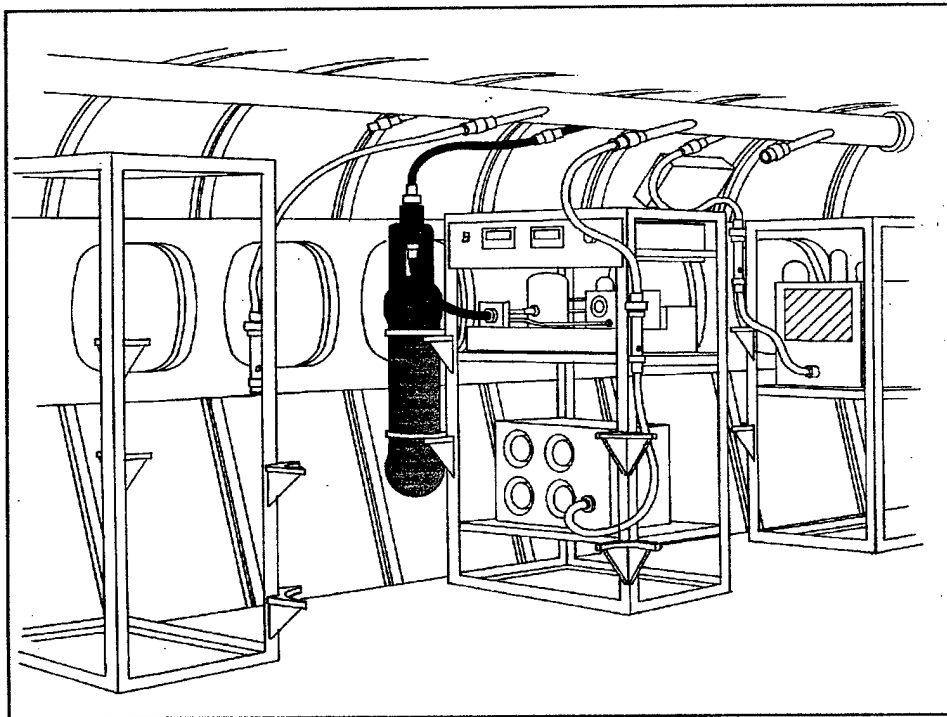


**Figure 6.** Conceptual drawing of an FSSP and inlet calibration device in the Navy Twin Otter research aircraft.

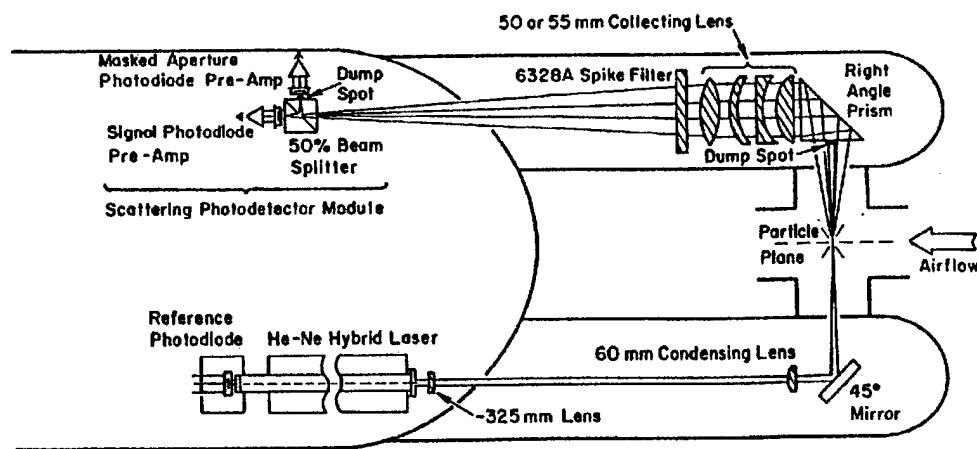


**Figure 7.** Optical layout of FSSP 100 taken from Baumgardner and Skinner (1989).

**Figure 8** is a Zemax ray trace of the optical system with the 0.5 mm thick sapphire window inserted between the sample volume and the prism. Physical measurements were taken of the SPEC FSSP 100 to determine focal lengths and lens spacings for the ray tracing analysis. The ray trace determines the path of the scattered light rays from the sample volume to the detector module. After passing through the sapphire window, the rays intersect the first surface of the prism, which also serves as the mounting surface for the dump spot. Rays at large enough angles (3 degrees or greater) scatter around the dump spot. The scattered light rays are bent 90 degrees by the folding prism. The optical path through the prism is shown unfolded in this case. After exiting the prism, the scattered light is received by the objective lens.

Unfortunately, no engineering data were available from Particle Measuring Systems (PMS), the original manufacturer of the probe, regarding the optical prescription for the four-element objective lens. Particle Metrics Incorporated (PMI), the current manufacture of the FSSP, did not have access to this information either. SPEC contacted other researchers who have used the FSSP and published their results, but none were aware of the details of the objective lens.

For this reason, the objective lens is modeled as a pair of paraxial lenses, with focal lengths equal to the front focal length and back focal length measured in the laboratory. A paraxial lens acts as perfect lens, in that no aberrations are present. The concept is valid for rays near the optical axis. For a well-corrected objective lens, this approach should be reasonable. From the laboratory measurements, the front focal length (ffl) =

59 mm and the back focal length (bfl) = 193 mm. The length of the objective was 40 mm. To determine the overall focal length of the combined system

$$f_{ab} = \frac{f_a f_b}{f_a + f_b - d}$$

where  $f_{ab}$  is the combined focal length,  $f_a$ =ffl,  $f_b$ =bfl, and  $d$  is the separation between the lenses. In this case  $f_{ab}$ =53 mm. This is very close to the 55 mm focal length quoted by PMS.

After exiting the objective lens, the light is focused onto the photodetector module. In this case, the signal detector is of greatest interest because the intensity of light hitting the signal detector determines the particle size. To determine the effect of the sapphire window, the ray trace was performed with and without the window in place.

The minimum detected angle is determined by the size of the dump spot, while the clear aperture of the objective lens determines the maximum detected angle. The diameter of the dump spot is measured to be 4 mm while the aperture of the objective lens is measured to be 25.2 mm. If only the first order effect of shifting the focus of the system is considered, the collection angles remain the same. For the particular geometry modeled here, the FSSP collects light scattered between half angles of 3 degrees and 12 degrees. The angles are determined by looking at the particular angle of the rays passing outside of the dump spot and within the aperture of the lens using the Zemax spot diagram function at various surfaces.

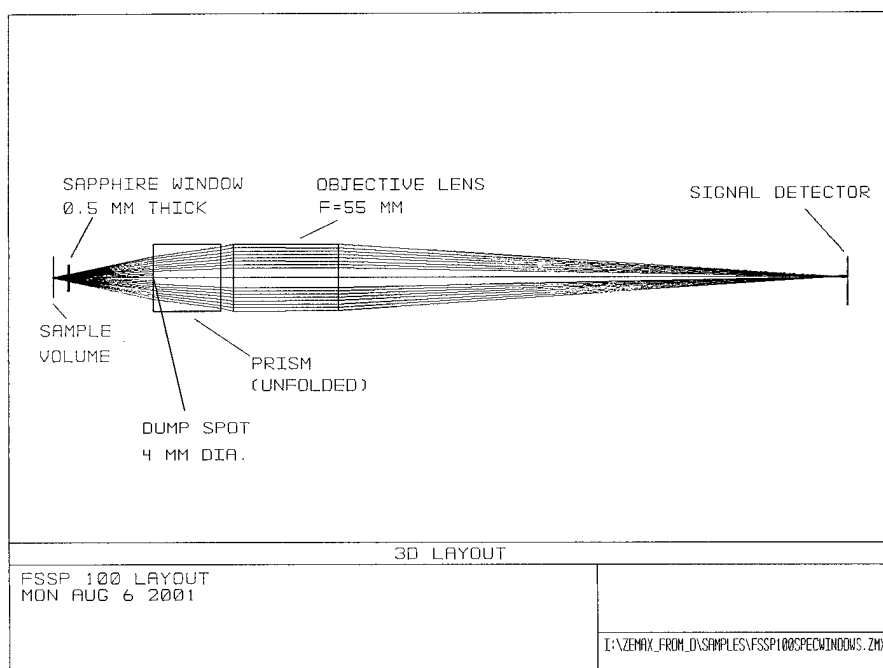


**Figure 8.** Zemax ray trace of FSSP 100 optical system with sapphire window inserted.

If the shift in focus is not considered, then the collection angle changes from 3 – 12 degrees to 3.02 – 12.04 degrees for particles passing exactly through the center of the sample tube. Table I is a summary of these angles.

	<i>Minimum half angle collected (degrees)</i>	<i>Maximum half angle collected (degrees)</i>
<i>Window absent</i>	<b>3</b>	<b>12</b>
<i>Window present</i>	<b>3.02</b>	<b>12.04</b>

**Table I.** Change in collection angle by adding 0.5 mm thick sapphire window.

The next step in the analysis is to calculate the integrated light intensity hitting the detector for both geometries based on Mie theory. SPEC has developed a numerical model based on Mie theory used to study light scattering from spherical particles. The model has been used in the design and analysis of a number of instruments developed at SPEC including the Cloud Particle Imager (CPI) and Cloud Extinctionmeter.

**Figure 9** is a plot of droplet diameter versus relative scattering intensity for both sets of angles. The model was validated by comparing the output to results generated by Dye and Baumgardner (1984) for angles of 3 – 12.7 degrees. The results were in excellent agreement. **Figure 10** shows the difference in the curves for the angles being considered for the SPEC FSSP 100.

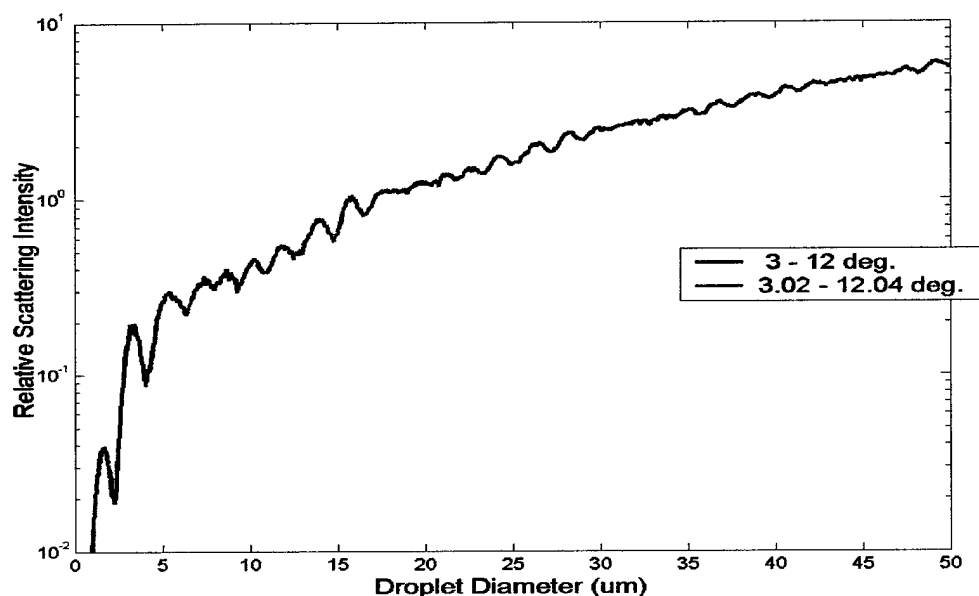


**Figure 9.** Droplet diameter versus relative scattering intensity for cases with and without sapphire window.

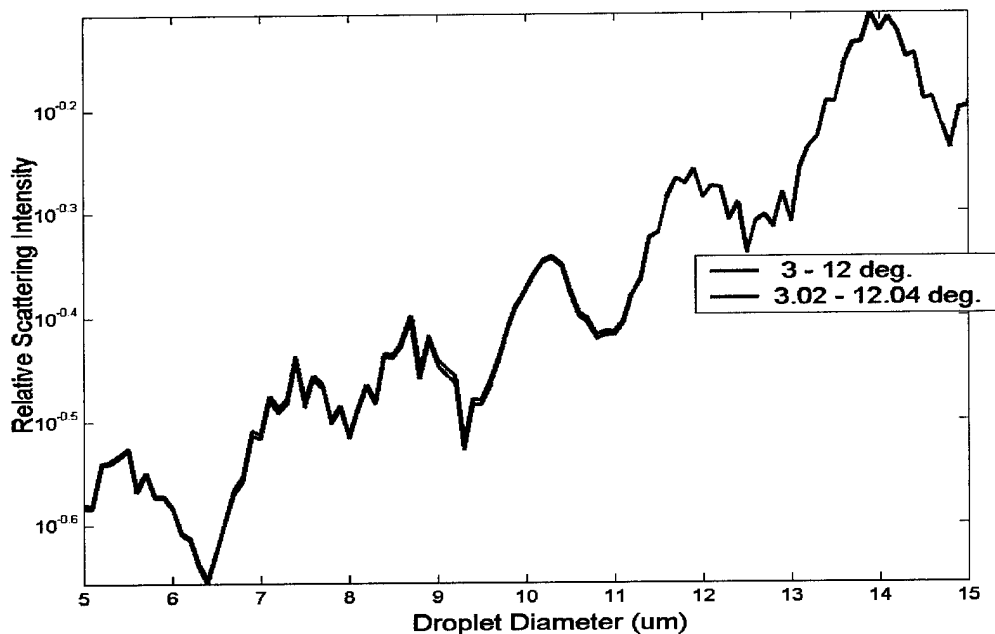


**Figure 10.** Expanded scale of droplet diameter versus relative scattering intensity.

**Figure 10** shows very little difference for the integrated scattering intensity due to increasing the collection angles from 3 – 12 degrees to 3.02 – 12.04 degrees. The results of the optical simulations indicate that the addition of the sapphire window into the collection optics will not have a significant effect on the performance of the instrument due to changing the collection angles.

### 3.3 Design and Fabrication of a Prototype Inlet Calibration Device

The mechanical components of the inlet calibration device were designed using the Solidworks™ CAD software package. As shown in **Figure 5**, a precision translation stage was integrated into the calibrator so that the position of the internal tube can be moved across the viewing area of the FSSP. By moving the internal tube across the viewing area, it was possible to measure aerosol size distribution from the middle out to the walls of the tube. Since velocity distribution in a tube is well known for the range (300 to 3000) of Reynolds numbers encountered in the actual application, the measurement of total volume flow at the exit of the tube will provide the required closure to determine absolute particle size distribution.

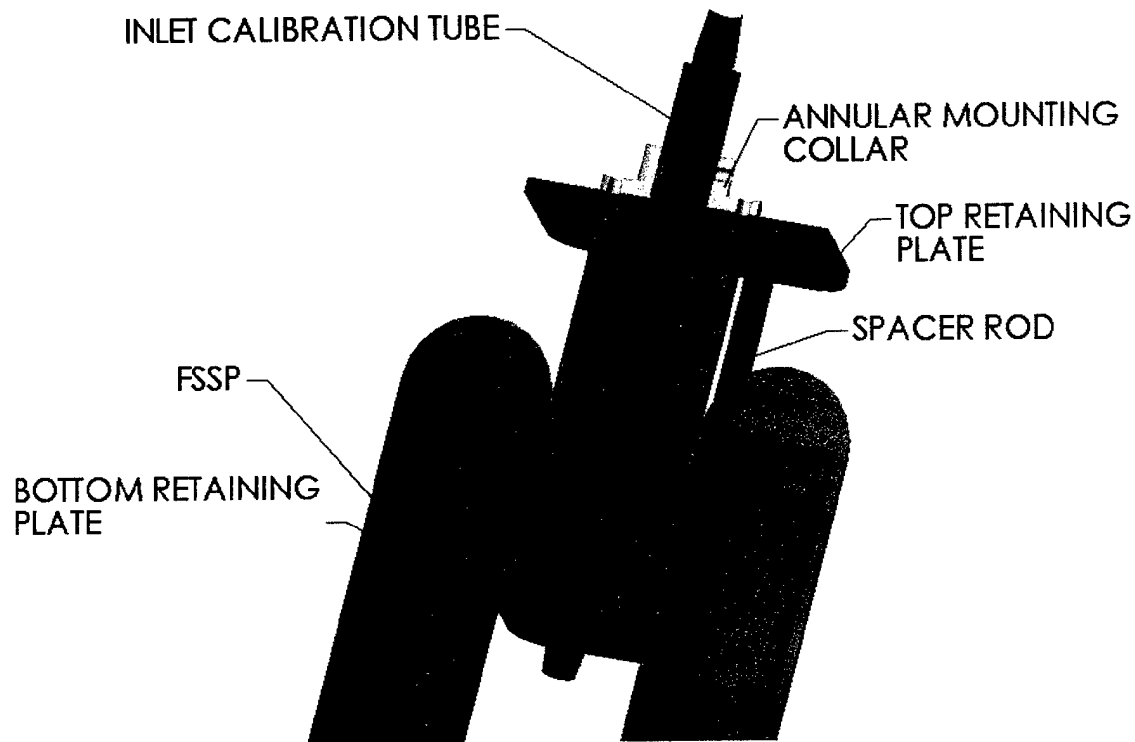


**Figure 11.** Cutaway view of assembled inlet calibration device.

**Figure 11** is a Solidworks™ assembly drawing of the inlet calibration device. The device consists of a top and bottom retaining plate that bolt onto the FSSP sample tube using spacer rods. The inlet tube is then mounted to the top plate using an annular mounting collar. The top retaining plate has been designed to interface with an off the shelf translation stage. **Figure 12** is a photograph of the actual inlet calibration device without the inlet tube installed. Notice that the translation stage is installed in **Figure 12**.

**Figure 13** is a photograph of the actual inlet tube. The tube has been irridited to maintain electrical conductivity between the two conductive tubes that will be attached to either end for the actual application. The idea was to prevent the particles from sticking to the walls of the tube. Black anodizing the inlet tube would have been preferable to minimize light scattering, but anodization acts as an electrical insulator. **Figure 14** is a mechanical drawing of the inlet tube for 11 mm ID tubing. Due to the overall length, the tube was manufactured in two halves that were threaded and screwed together. The internal diameters of the two halves were made to the exact dimension and the external diameter was turned in a lathe after the pieces had been screwed together.

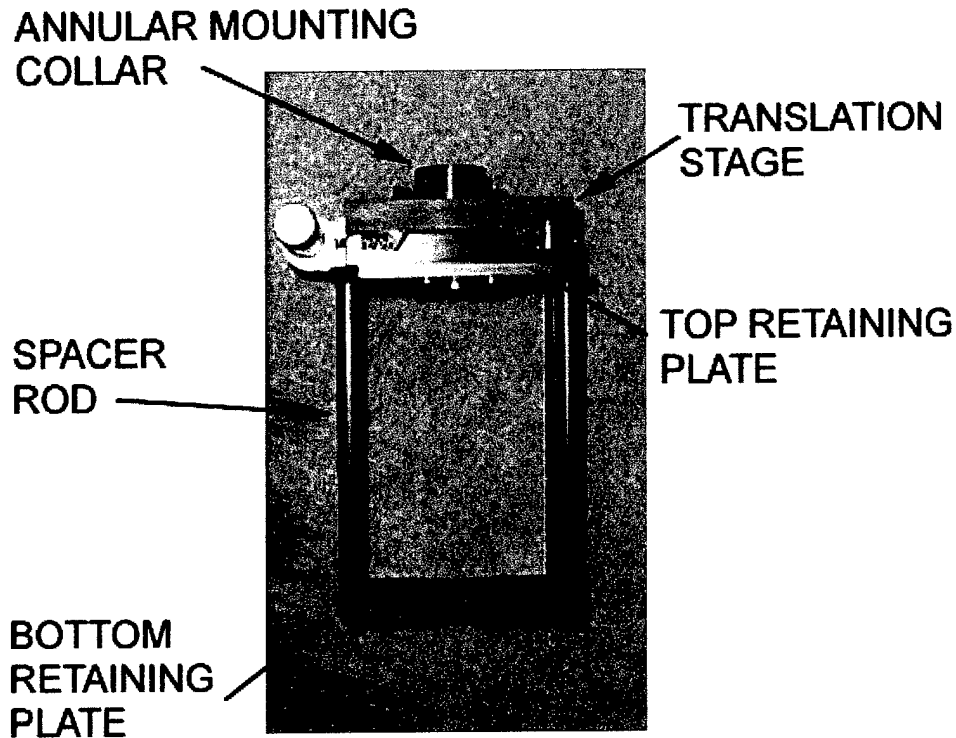


**Figure 12.** Inlet calibration device without inlet tube installed.

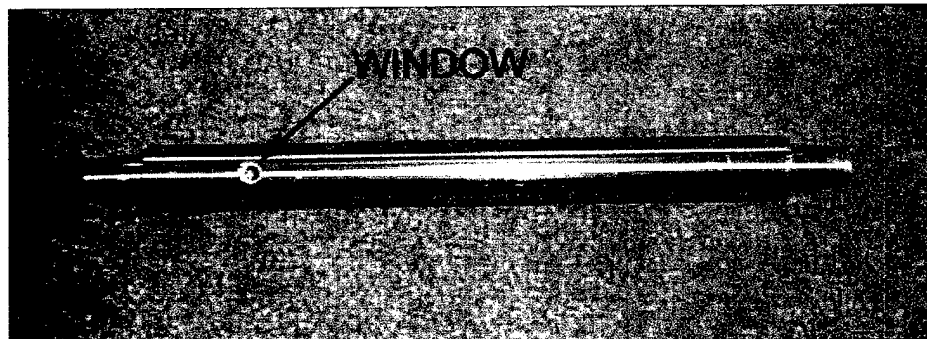


**Figure 13.** Inlet calibration tube showing location of windows.

**Figure 15** shows a closeup of the sapphire windows mounted into the tube. As stated in the previous section, the windows are 0.5 mm thick. The windows were anti-reflection (AR) coated to have a reflective surface loss of less than 0.1% per surface at 633 nm. **Figure 16** is a reflectance curve generated by the coating vendor, Spectrum Thin Films. The curve plots wavelength versus % reflectance and shows that the reflectivity per surface is much less than 0.1% at 633 nm.





Eccobond 286 epoxy was used to bond the windows into the inlet tube. **Figure 14 detail B** shows the milled counterbores into which the windows mount. A small amount of epoxy is placed into the counterbore and the window is pressed in. Care must be taken to keep the epoxy from flowing into the clear aperture of the window. SPEC has successfully used this bonding technique on other instruments. This technique results in mounting the windows parallel to one another and creating a pressure seal between the window and the aluminum tube. The pressure seal will be necessary to operate the inlet calibration device in its intended manner, having a stream of particles pulled through with a vacuum pump.

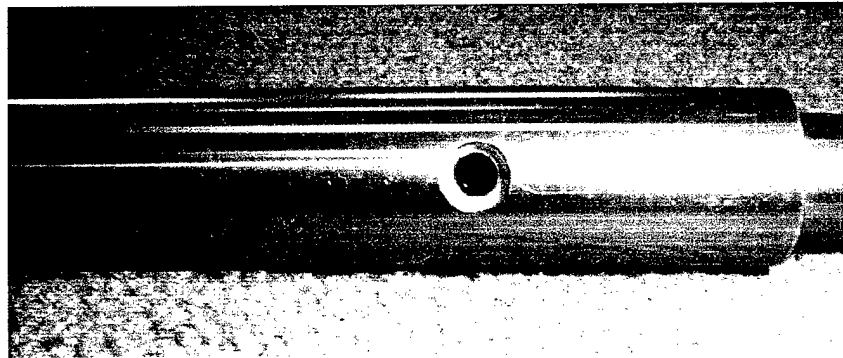


**Figure 15.** Close up of sapphire windows mounted into inlet tube.

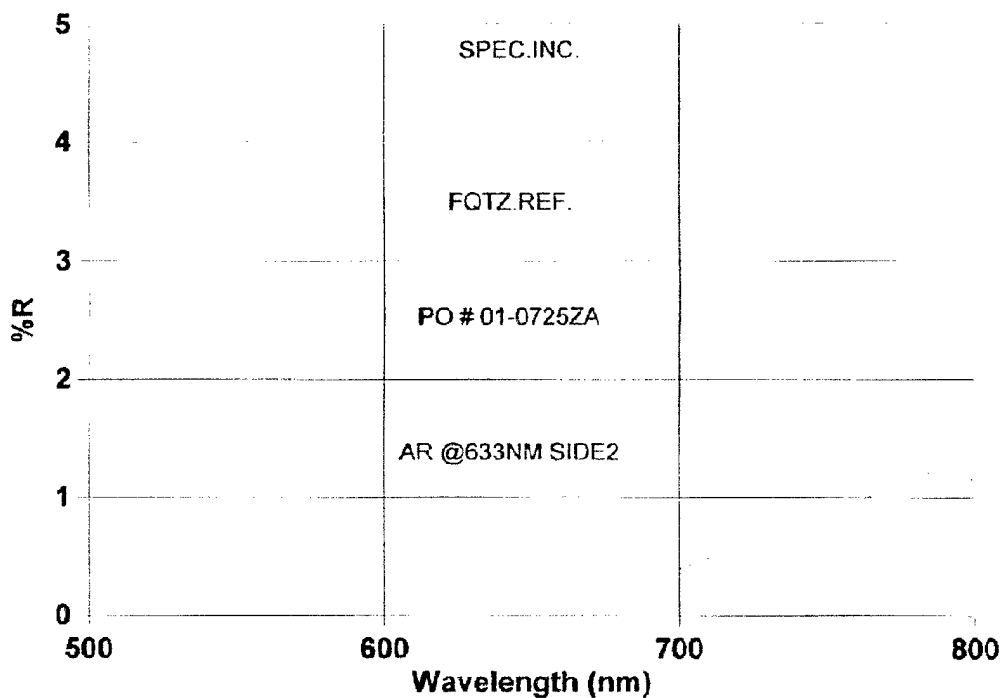


**Figure 16.** Reflectance curve for AR coating on Sapphire windows. Curve provided by Spectrum Thin Films.

The inlet and outlet tubing will be coupled to the inlet tube by sliding the square cut ends of the tubing over the tapered ends of the inlet tube. Initially, mating the tubing to the inlet device was going to be accomplished using custom designed fittings. This new approach is conceptually much simpler. The gradual taper in the inlet tube prevents an abrupt step change in the flow from the 11 mm conductive tubing into the inlet tube, thereby reducing any turbulence that may be generated by the step change. The gradual taper of the outside diameter increases to where the conductive tubing expands and forms an airtight seal between the inlet tube and the conductive tubing. **Figure 17** is a photograph of the end of the inlet tube showing the tapered section. The mechanical details of this design are shown in **Figure 14 Detail C**.



**Figure 17.** Close up view of tapered end of inlet tube.

A drawback of this particular design was discovered during testing. The lip of the tube is a very sharp thin section of aluminum. As a result, the thin aluminum is easily deformed when sliding a tube on and off. This results in irregularities in the surface which may create turbulence in the tube. A few possibilities exist to try and solve this problem in the future. A different alloy aluminum can be used which is harder and more resistant to deformation. Al 6061-T6 was used to build the inlet tube. Both Al 7075-T6 and Al 2024-T6 have a higher Brinell hardness than Al 6061-T6 (150 and 120 compared to 95). Using a harder alloy would improve the resistance of the lip to deformation. The other possibility would be to have a very small step, thereby increasing the thickness of the lip. A third possibility would be to use another material such as stainless steel, which is much harder than Al. It is also more costly and difficult to machine.

**Figure 18** is a photograph of the entire assembly installed in the SPEC FSSP-100. The assembly pictured in **Figure 12** is first mounted by removing the bottom retaining plate and sliding in onto the FSSP sample tube. The top retaining plate has a small boss protruding that fits tightly into the FSSP sample tube and centers the assembly. The bottom retaining plate is then screwed back on to make the assembly captive to the FSSP. The inlet tube is inserted into the annular mounting ring and held in place

using two set screws. The inlet tube is registered to the proper alignment and position by aligning a radial and vertical mark on the inlet with similar marks on the annular mounting collar. These registration marks were added after the tube was manufactured. In the future two sets of these marks will be machined onto the inlet tube. One set will be to register the inlet tube when the translation stage is present, the other set will be to register the tube when the translation stage is not installed.

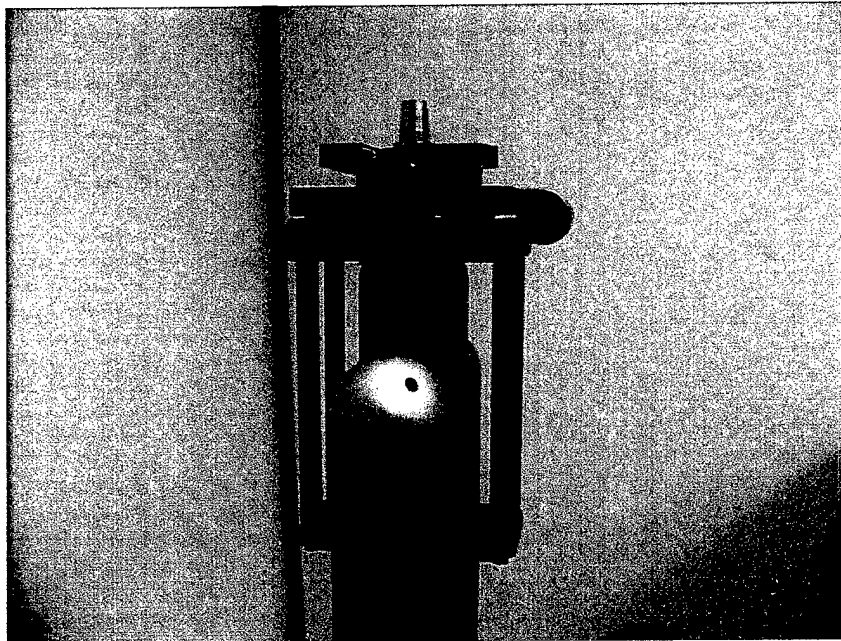


**Figure 18.** Inlet calibration device assembly installed on SPEC FSSP-100.

### **3.4 Testing of the Prototype in the Laboratory**

#### **3.4.1 Laboratory Set Up**

Testing of the inlet calibration device was performed in the laboratory using the SPEC FSSP-100. The purpose of the tests was to determine the effect of the inlet calibration device on sizing measurements made by the FSSP. A vacuum cleaner was used to aspirate the FSSP and provide flow through the sample volume. Glass beads were passed through the sample volume and sized with and without the calibration insert installed. The SPEC 1D interface card was used to connect the FSSP to a PC data system. Real-time software written by SPEC was used to collect and record the data from the FSSP.

The FSSP has four size ranges. The size limits for each range are given in **Table II**. These are nominal size ranges specified by the manufacturer. The FSSP sizes particles into one of fifteen size bins for each of these ranges. The size of each of the bins in a particular range is constant, and given in **Table II**. **Table III** lists the minimum

and maximum particle size for each bin of each range used for these experiments as well as the median size for each bin in each range. The optical specifications for the SPEC FSSP-100 are given in **Section 3.2**. The nominal beam diameter is 0.2 mm and the depth of field is between 2 and 3 mm. The exact numbers are not relevant for this study because the purpose is to determine the specific effects on the FSSP measurements, if any, that are introduced by the inlet calibration device. Any sizing errors or improper calibrations inherent in the FSSP itself remain present independent of the inlet calibration device.

The FSSP-100 was operated over all of the size ranges during the laboratory experiments. However, ranges 0 and 1, which are the ranges that most researchers operate the FSSP-100, were the primary size ranges used in this experiment to evaluate the inlet calibration device. Due to a number of factors, such as the “bumps” in the Mie curve, high sensitivity to room aerosols and noise, etc., the FSSP-100 data in size ranges 2 and 3 are not as reliable as the data collected in size ranges 0 and 1. Also, it is very difficult to work with glass beads less than 8  $\mu\text{m}$  in diameter because they tend to clump and they are generally only available in a suspension. Some limited laboratory data from size range 2 are shown in this report to illustrate the effect of contamination from room aerosols and noise. The FSSP-300 is a more reliable instrument that should be used to make measurements of particles  $< \sim 5 \mu\text{m}$  in diameter.

Size Range #	Particle size range ( $\mu\text{m}$ )	Bin width ( $\mu\text{m}$ )
0	2.0 – 47.0	3
1	2.0 – 32.0	2
2	1.0 – 16.0	1
3	0.5 – 8.0	0.5

**Table II.** FSSP-100 size range parameters.

**Table IV** lists the sizes of glass microspheres used for the experiments. The microspheres are purchased from Duke Scientific Corporation, who is a leader in the industry of manufacturing particles size standards. The primary sizes of beads used for these experiments are 10  $\mu\text{m}$ , 14.5  $\mu\text{m}$ , 20  $\mu\text{m}$ , and 40  $\mu\text{m}$ . These sizes provide good coverage of the FSSP size ranges 0 to 1.

Due to the difference in the index of refraction of glass compared to water (1.51 versus 1.33), the FSSP sizes glass microspheres differently than it sizes water drops. **Figure 19** is a plot of sphere diameter versus relative scattering intensity for water spheres and glass spheres. From this plot, it is seen that the FSSP will undersize glass beads. Looking at **Figure 19**, a glass microsphere with a diameter of approximately 20  $\mu\text{m}$  will have the same scattering intensity as a water drop of approximately 16 – 17  $\mu\text{m}$ . **Table V** is a list of equivalent water drop diameters for given glass bead sizes. This information was obtained from Droplet Measurement Technologies, Inc., who uses

these conversion values to calibrate particle sizing probes. The equivalent water drop diameters are derived from a curve similar to the one below.

B in #	Range 0		Range 1		Range 2	
	Size limits ( $\mu\text{m}$ )	Median size ( $\mu\text{m}$ )	Size limits ( $\mu\text{m}$ )	Median size ( $\mu\text{m}$ )	Size limits ( $\mu\text{m}$ )	Median size ( $\mu\text{m}$ )
1	2.0 – 5.0	3.5	2.0 – 4.0	3	1.0-2.0	1.5
2	5.0 – 8.0	6.5	4.0 – 6.0	5	2.0-3.0	2.5
3	8.0 – 11.0	9.5	6.0 – 8.0	7	3.0-4.0	3.5
4	11.0 – 14.0	12.5	8.0 – 10.0	9	4.0-5.0	4.5
5	14.0 – 17.0	15.5	10.0 – 12.0	11	5.0-6.0	5.5
6	17.0 – 20.0	18.5	12.0 – 14.0	13	6.0-7.0	6.5
7	20.0 – 23.0	21.5	14.0 – 16.0	15	7.0-8.0	7.5
8	23.0 – 26.0	24.5	16.0 – 18.0	17	8.0-9.0	8.5
9	26.0 – 29.0	27.5	18.0 – 20.0	19	9.0-10.0	9.5
10	29.0 – 32.0	30.5	20.0 – 22.0	21	10.0 – 11.0	10.5
11	32.0 – 35.0	33.5	22.0 – 24.0	23	11.0 – 12.0	11.5
12	35.0 – 38.0	36.5	24.0 – 26.0	25	12.0 – 13.0	12.5
13	38.0 – 41.0	39.5	26.0 – 28.0	27	13.0 – 14.0	13.5
14	41.0 – 44.0	42.5	28.0 – 30.0	29	14.0 – 15.0	14.5
15	44.0 – 47.0	45.5	30.0 – 32.0	31	15.0 – 16.0	15.5

**Table III.** Size limits and median size for each bin listed by FSSP range.

Nominal Diameter ( $\mu\text{m}$ )	Minimum Diameter ( $\mu\text{m}$ )	Maximum Diameter ( $\mu\text{m}$ )	Standard Deviation ( $\mu\text{m}$ )	Coefficient Of Variance (%)	Material	Index of Refraction (N) @589 nm
10 $\pm$ 1	9	11	1.4	15	Borosilicate glass	1.51
14.5 $\pm$ 1	13.5	15.5	4.7	12	Borosilicate glass	1.51
20.6 $\pm$ 1.4	19.2	22	1.9	9.4	Soda Lime glass	1.56
40 $\pm$ 2.8	37.2	42.8	2.4	4.9	Soda Lime glass	1.56

**Table IV.** Specifications of glass beads used for laboratory experiments. Beads purchased from Duke Scientific Corporation.

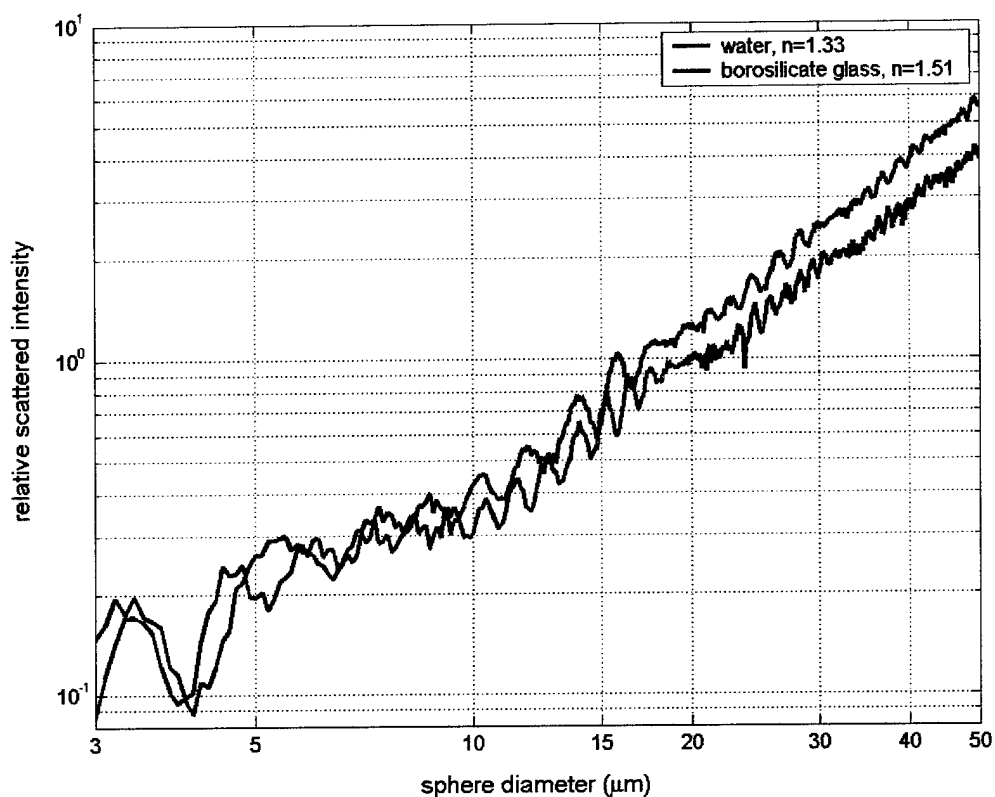


**Figure 19.** Comparison of sphere diameter versus relative scattering intensity for water drops and glass beads.

Glass Bead Diameter ( $\mu\text{m}$ )	Water Drop Diameter ( $\mu\text{m}$ )	Glass Bead Diameter ( $\mu\text{m}$ )	Water Drop Diameter ( $\mu\text{m}$ )	Glass Bead Diameter ( $\mu\text{m}$ )	Water Drop Diameter ( $\mu\text{m}$ )	Glass Bead Diameter ( $\mu\text{m}$ )	Water Drop Diameter ( $\mu\text{m}$ )
5	4.5	12	10.3	19	15.7	35	28.3
5.5	5	12.5	10.8	19.5	16.1	36	29
6	5.2	13	11.2	20	16.1	36.5	29.4
6.5	5.5	13.5	11.6	20.5	16.5	37	29.8
7	5.8	14	12	21	17	37.5	30.3
7.5	6	14.5	12.5	21.5	17.4	38	30.7
8	6.2	15	12.8	22	17.8	38.5	31.1
8.5	6.6	15.5	13.2	22.5	18.2	39	31.5
9	7.3	16	13.6	23	18.6	40	32.5
9.5	8.1	16.5	13.9	23.5	19	41	33.3
10	8.9	17	14.3	24	19.4	42	34.1
10.5	9.1	17.5	14.7	24.5	20	42.5	34.5
11	9.5	18	14.9	25	20.4	43	34.9
11.5	9.9	18.5	15.3	30	24.4	44	35.7

**Table V.** Equivalent water drop diameter for various glass bead diameters.

Beads were delivered to the FSSP by dispensing a small amount of beads into the cap for each of the particular jars containing the beads. The cap would then be placed by hand near the lip of the inlet tube or the edge of the FSSP sample volume if the inlet was not present. The lid would gradually be tipped on its side until the beads were being sucked out by the flow through the FSSP. Pouring the beads directly into the FSSP was avoided in order to minimize coincidence in the sample volume. Instead, the beads would get sucked out of the lid as it was held sideways.

Particle size histograms were recorded for three separate configurations. The first configuration consisted of the FSSP aspirated with the vacuum cleaner, without the inlet calibration tube installed. The vacuum was inserted into the backside of the FSSP sample tube. The second configuration consisted of the FSSP aspirated with the vacuum cleaner, with the inlet calibration tube installed. Again, the vacuum was inserted into the backside of the FSSP sample tube. The third configuration consisted of the FSSP with the inlet calibration tube installed, and a tube attached to the vacuum cleaner pulling particles directly through the inlet calibration tube. **Figure 20** is a photograph showing this third experimental configuration. The third configuration is the one that most accurately matches the application for the device when it is used to calibrate aerosol inlets. In this configuration, all air and particles flow through the inlet calibration device. The velocity through the inlet calibration device will be higher in this case than in the second configuration because the cross-sectional flow area is smaller.

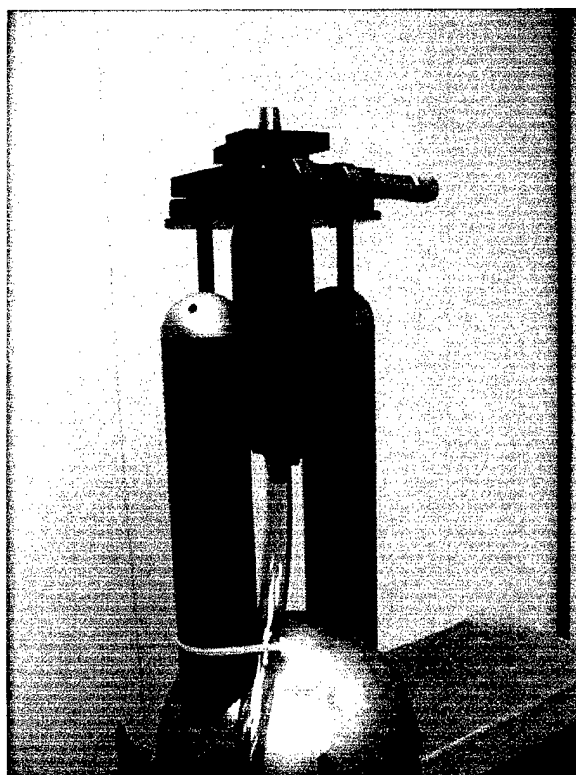


**Figure 20.** FSSP-100 with inlet calibration insert installed and aspiration tube attached to inlet tube. For the other experimental configurations, the vacuum is inserted directly into the FSSP sample tube.



### 3.4.2 Results with FSSP operating on Range 0

**Figure 21** is a plot of four bead size histograms generated in the first experimental configuration with the FSSP set on size range 0. Each histogram is calculated by summing all the particles collected over the time that the beads were being dispensed. Due to the lack of reproducibility involved in dispensing the beads, data were collected until a statistically representative histogram could be accumulated. The red lines plotted on each of the histograms represent the minimum and maximum equivalent water drop sizes that were possible given the tolerance on the mean diameter for the glass microspheres. For example, **Table IV** shows that 10  $\mu\text{m}$  beads can have a mean diameter ranging from 9 – 11  $\mu\text{m}$ . Looking at **Table V**, this corresponds to equivalent water drop sizes ranging from 7.3 – 9.5  $\mu\text{m}$ . The lines plotted in the upper left histogram of **Figure 21** are at 7.3  $\mu\text{m}$  and 9.5  $\mu\text{m}$ , corresponding to the range of bead sizes to be expected. The highlighted areas in **Table V** correspond to the appropriate equivalent water drop diameters for the glass beads used in these experiments.

**Figure 21a – 21c**, corresponding to 10  $\mu\text{m}$ , 14.5  $\mu\text{m}$ , and 20  $\mu\text{m}$  glass beads respectively, show the maximum number of beads falling into the size bin that is just at or below the lowest expected equivalent water drop diameter. **Figure 21d**, which plots the histogram for 40  $\mu\text{m}$  beads, shows a peak in the smallest size bin and a second peak in the bin below the lowest expected equivalent water drop diameter. The total counts are very low for the 40  $\mu\text{m}$  bead histogram. Part of the reason for the low counts is the difficulty in targeting the 40  $\mu\text{m}$  through the sample volume. The laser beam diameter is approximately 200  $\mu\text{m}$ , only five times the diameter of a 40  $\mu\text{m}$  bead. Both **Figures 21c** and **21d** show a number of counts in the smallest size bin. This may be due to the depth of field rejection not functioning correctly.

**Figure 22** shows data collected in the second experimental configuration with the FSSP operating on size range 0. The calibration insert is in place and the vacuum is connected to the FSSP sample tube. The counts are much higher in each of the four histograms. This is due to the improvement in targeting when dropping beads into the inlet calibration tube. All of the particles are restricted to the 11 mm diameter inlet tube in configuration two, compared to the 38 mm sample tube of the FSSP in configuration one. The total flow area decreases by a factor of twelve. For each of the four histograms, the bin with the most counts is exactly at, or slightly below, the expected equivalent water drop diameter.

**Figure 23** is a plot of data collected with the FSSP in the third experimental configuration. The inlet calibration device is present and a tube is pulling particles directly through the inlet tube as shown in **Figure 20**. This configuration most closely resembles the intended application for the inlet calibration device. The results from **Figures 23a-d** are very similar to the results from **Figure 22a-d**, with the highest number of counts occurring at, or slightly below, the expected equivalent water drop diameter. This is a strong indication that, as predicted by the Zemax ray-tracing

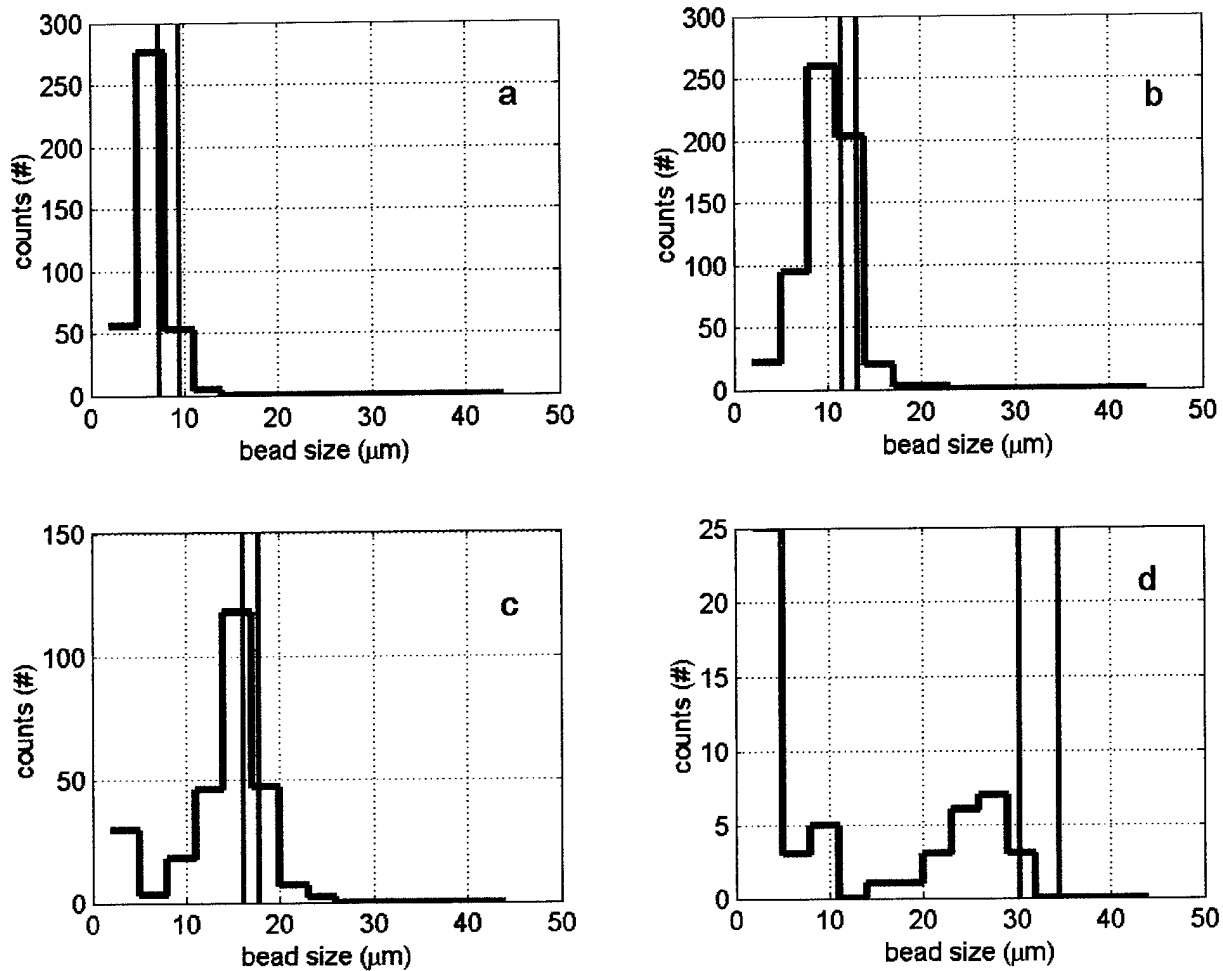


**Figure 21.** Bead size distributions measured by the FSSP on Range 0, without the calibration insert. A vacuum is used to aspirate the FSSP. The nominal bead diameter for each histogram is a.) 10 μm, b.) 14.5 μm, c.) 20 μm, and d.) 40 μm.

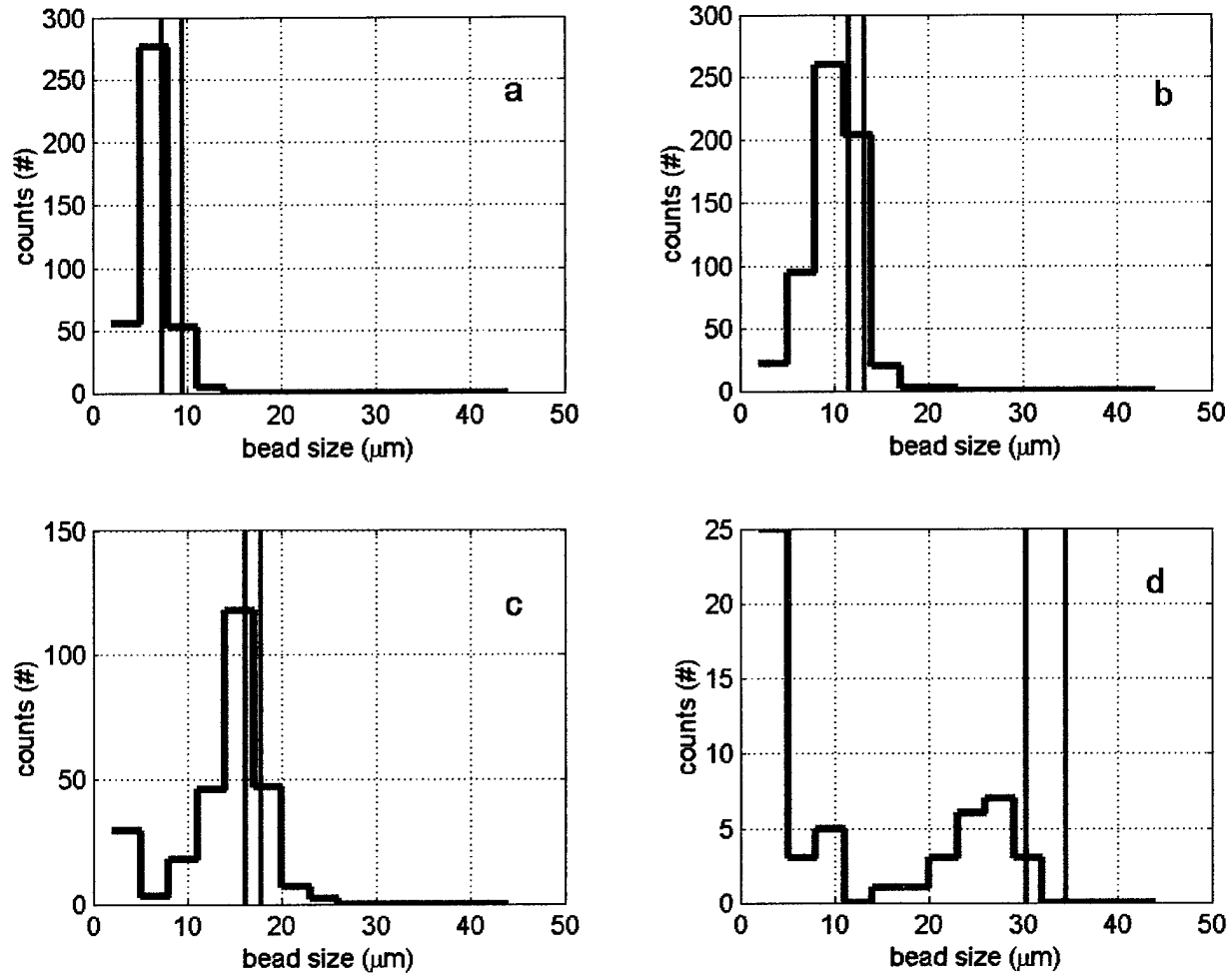


**Figure 22.** Bead size distributions measured by the FSSP on Range 0, with the calibration insert. A vacuum is used to aspirate the FSSP. The nominal bead diameter for each histogram is a.) 10  $\mu\text{m}$ , b.) 14.5  $\mu\text{m}$ , c.) 20  $\mu\text{m}$ , and d.) 40  $\mu\text{m}$ .

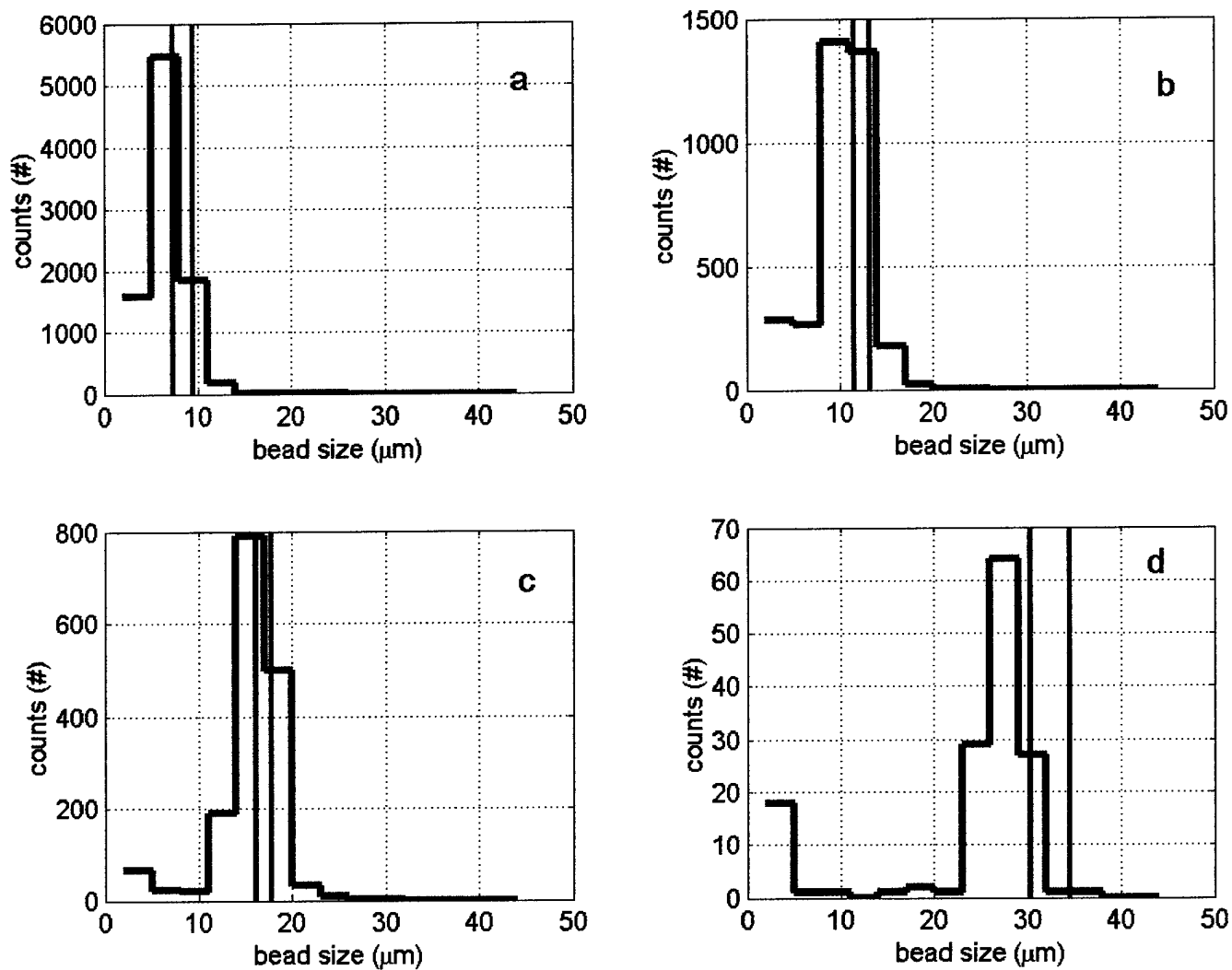


**Figure 23.** Bead size distributions measured by the FSSP on Range 0, with the calibration insert and the aspiration tube. The nominal bead diameter for each histogram is a.) 10  $\mu\text{m}$ , b.) 14.5  $\mu\text{m}$ , c.) 20  $\mu\text{m}$ , and d.) 40  $\mu\text{m}$ .

software, the windows in the inlet calibration device are not introducing a size bias into the FSSP-100. Notice the number of counts in the smallest size bin for **Figures 22c-d** and **Figures 23c-d**, possibly indicating that the transit-time particle rejection electronics are not working adequately at this slow airspeed.

### 3.4.3 Results with FSSP operating on Range 1

**Figures 24a-d, 25a-d, and 26a-d** are plots of histograms recorded with the FSSP operating on size range 1. 40  $\mu\text{m}$  beads are not used for these plots because they exceed the maximum measured particle size in this range. **Figure 24** corresponds to experimental configuration one (FSSP only), **Figure 25** corresponds to experimental configuration two (inlet tube installed), and **Figure 26** corresponds to experimental configuration three (inlet tube installed, aspirated through tube). All of the histograms in **Figures 24, 25, and 26** show the maximum number of counts appearing in the size bin exactly at, or just below the expected equivalent water drop diameter. Again, these results verify that the windows in the inlet calibration device are not having an appreciable effect on FSSP sizing.

### 3.4.4 Results with FSSP operating on Range 2

**Figures 27, 28, and 29** are plots of histograms recorded with the FSSP operating on size range 2. **Figure 27** corresponds to experimental configuration one (FSSP only), **Figure 28** corresponds to experimental configuration two (inlet tube installed), and **Figure 29** corresponds to experimental configuration three (inlet tube installed, aspirated through tube). For this round of experiments, only 10  $\mu\text{m}$  and 14.5  $\mu\text{m}$  beads are within the minimum and maximum particle size limits. **Figures 27a** and **27b** are for 10  $\mu\text{m}$  and 14.5  $\mu\text{m}$  respectively, and **Figures 27c** and **27d** zoom in on the y-axis for these same two histograms.

**Figure 27** shows a very high number of counts in the lowest size bin for the case of no inlet installed. Compared to this configuration in the other size ranges, the number of counts in this first bin significantly outnumbers the particles recorded in the other bins. During the experiment many counts were present in this bin even when no particles were being introduced to the sample volume. There are at least two possible causes for the measurements in the first size bin. One of the possible causes is that the instrument is actually measuring aerosols that are in the room air in the 1.0 - 2.0  $\mu\text{m}$  size range. The other possible cause is that optical and electronic noise creates a high enough signal on the detectors to be measured as a particle. In order to measure smaller particles, each successively smaller size range uses a higher gain. **Figures 27c** and **27d** show that there are still a significant number of counts in the other size bins, indicating that the FSSP continues to properly size particles, even in the presence of noise contamination in bin 1. The peak number of counts for both bead sizes appears slightly smaller than the expected equivalent water drop diameter.

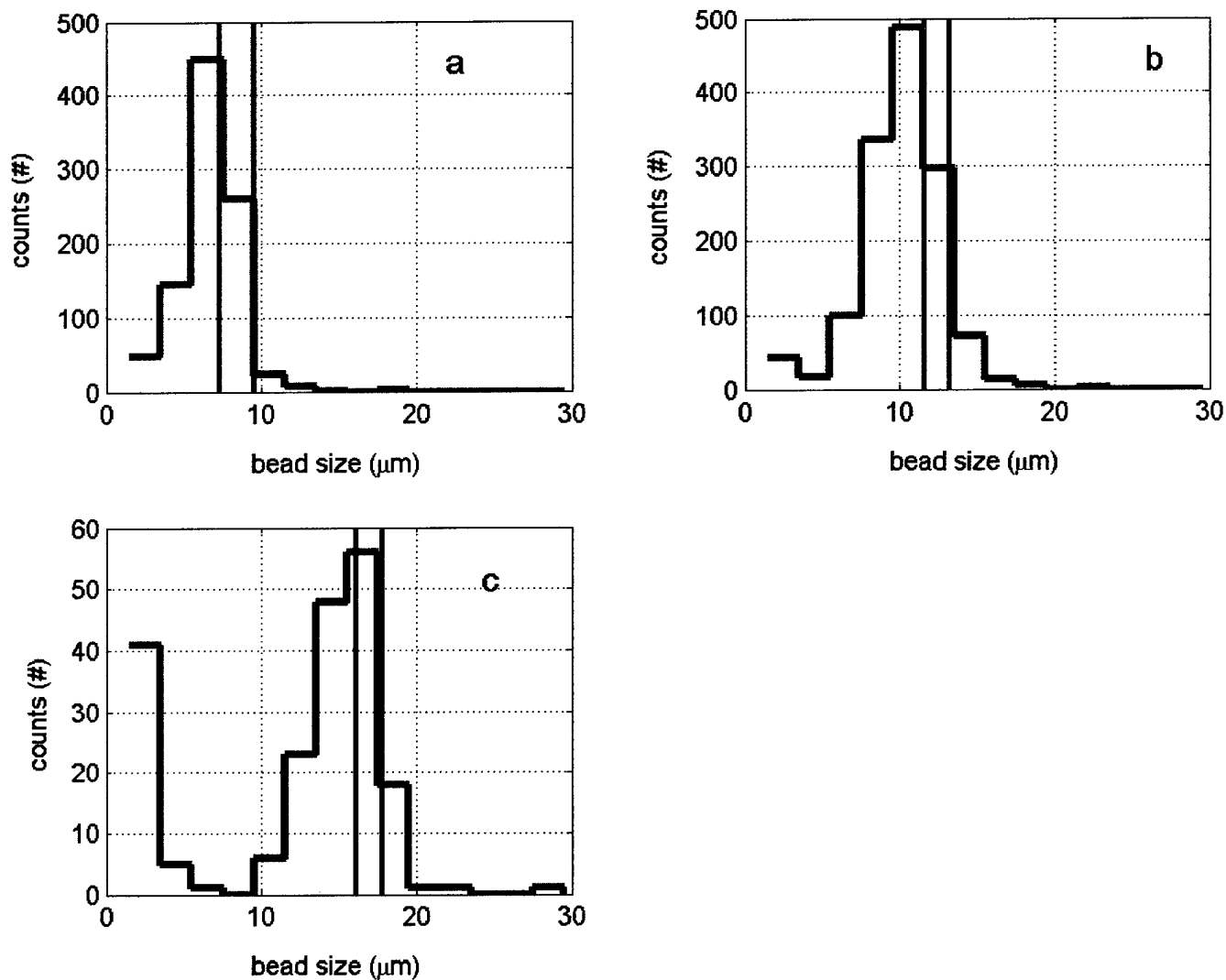


**Figure 24.** Bead size distributions measured by the FSSP on Range 1, without the calibration insert. A vacuum is used to aspirate the FSSP. The nominal bead diameter for each histogram is a.) 10 μm, b.) 14.5 μm, c.) 20 μm.

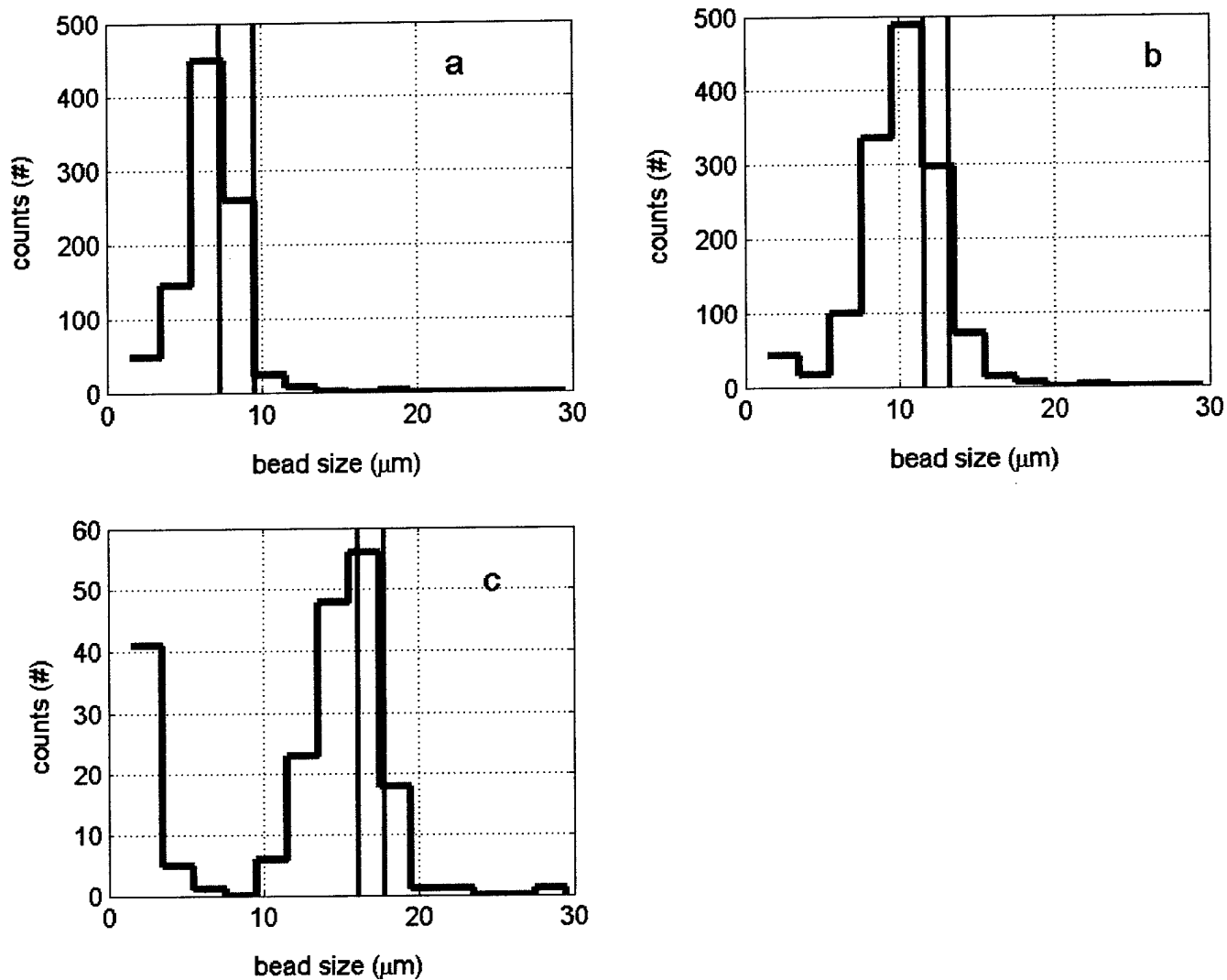


**Figure 25.** Bead size distributions measured by the FSSP on Range 1, with the calibration insert. A vacuum is used to aspirate the FSSP. The nominal bead diameter for each histogram is a.) 10 μm, b.) 14.5 μm, c.) 20 μm.

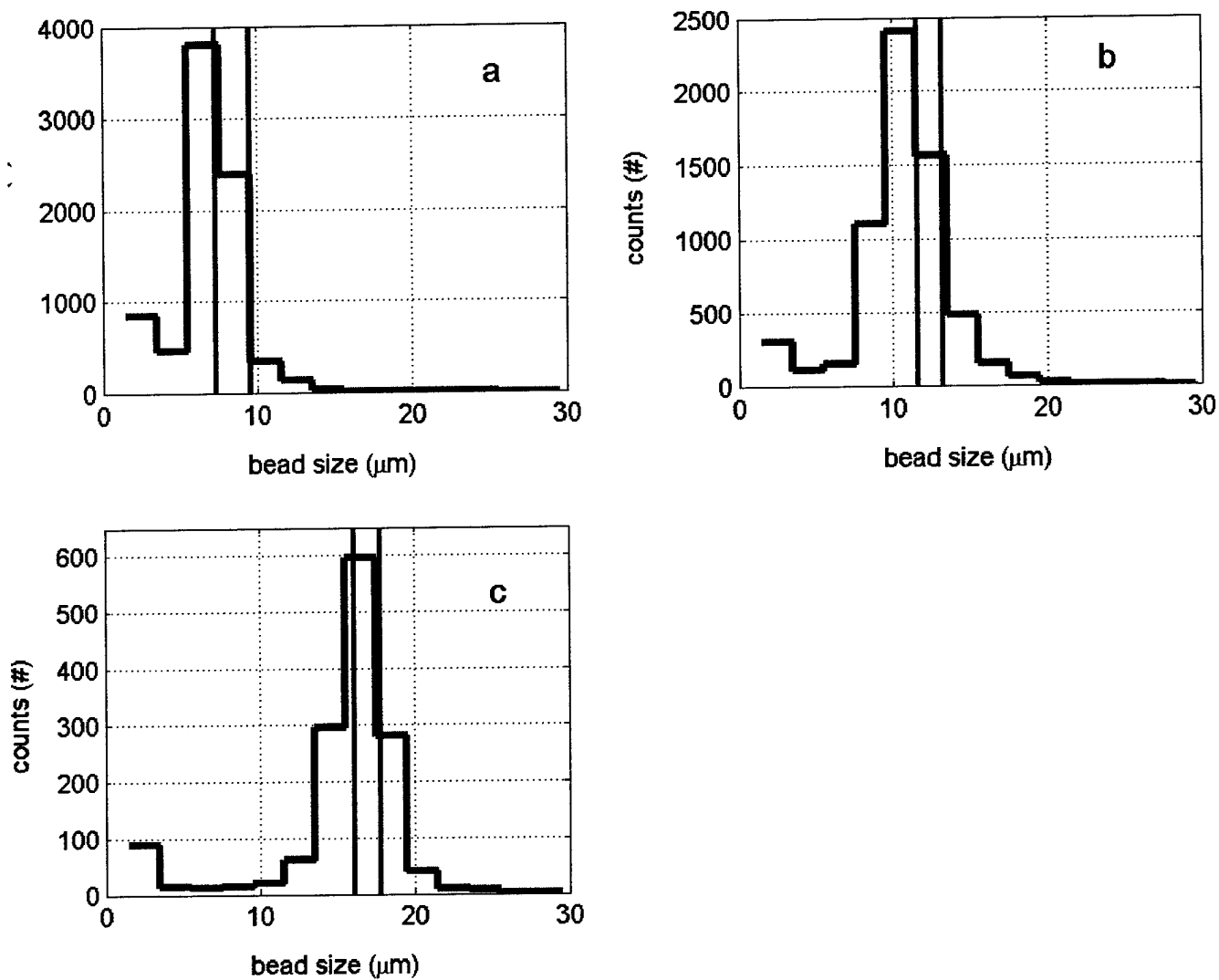


**Figure 26.** Bead size distributions measured by the FSSP on Range 1, with the calibration insert and the aspiration tube. The nominal bead diameter for each histogram is a.) 10 μm, b.) 14.5 μm, c.) 20 μm.



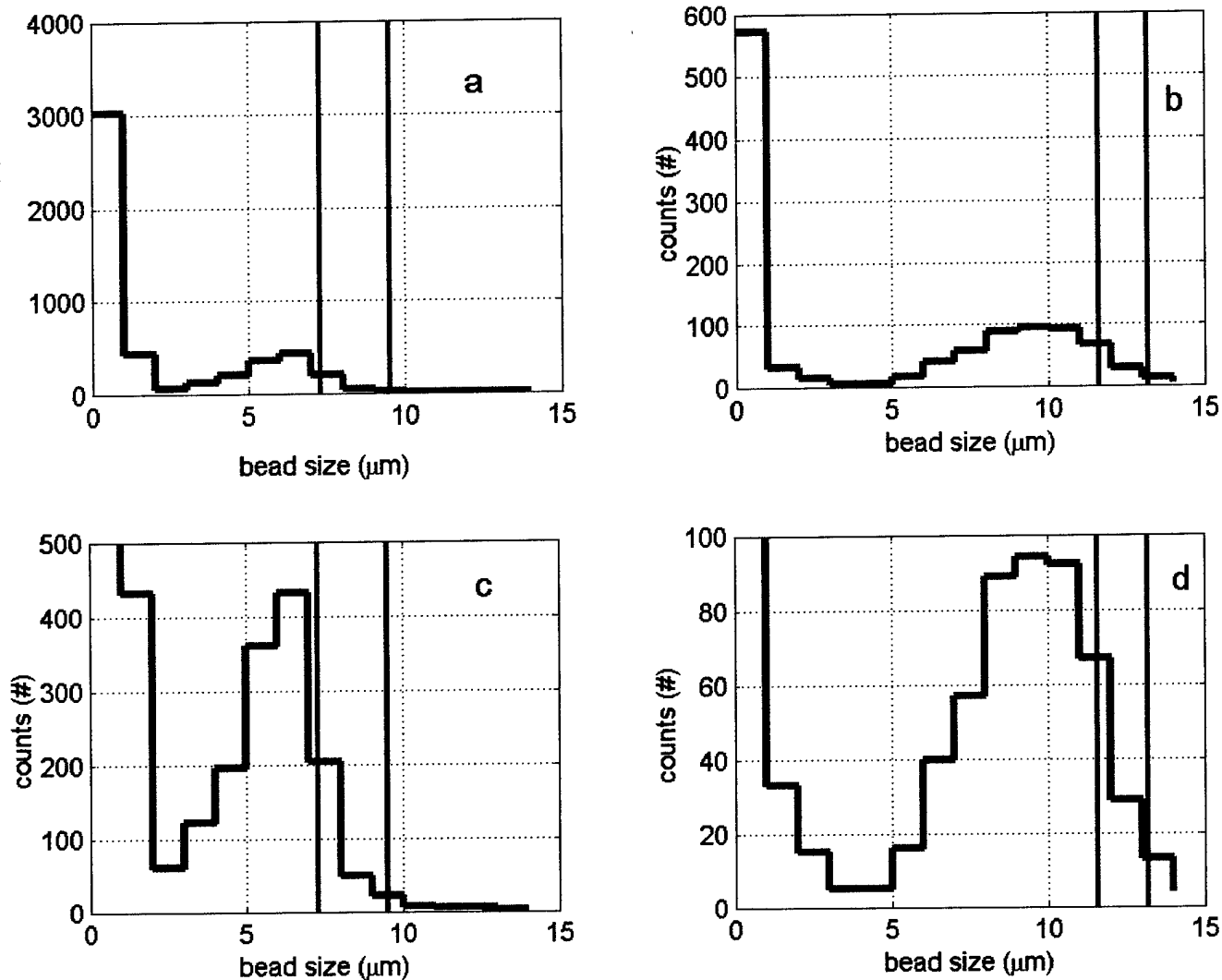


**Figure 27.** Bead size distributions measured by the FSSP on Range 2, without the calibration insert. The nominal bead diameter for each histogram is a.) 10  $\mu\text{m}$ , b.) 14.5  $\mu\text{m}$ , c.) 10  $\mu\text{m}$  expanded scale, and d.) 14.5  $\mu\text{m}$  expanded scale.

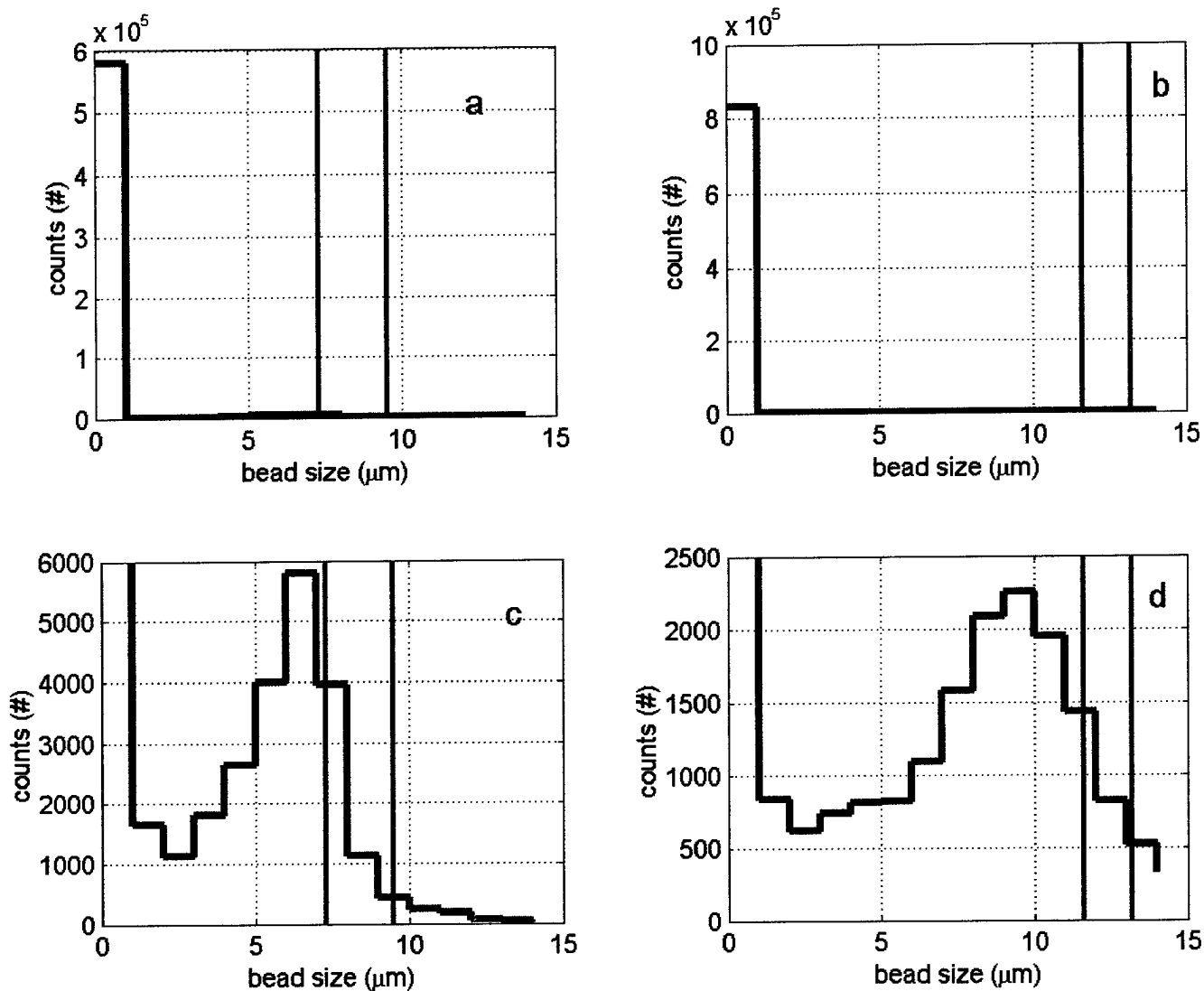


**Figure 28.** Bead size distributions measured by the FSSP on Range 2, with the calibration insert. The nominal bead diameter for each histogram is a.) 10 μm, b.) 14.5 μm, c.) 10 μm expanded scale, and d.) 14.5 μm expanded scale.

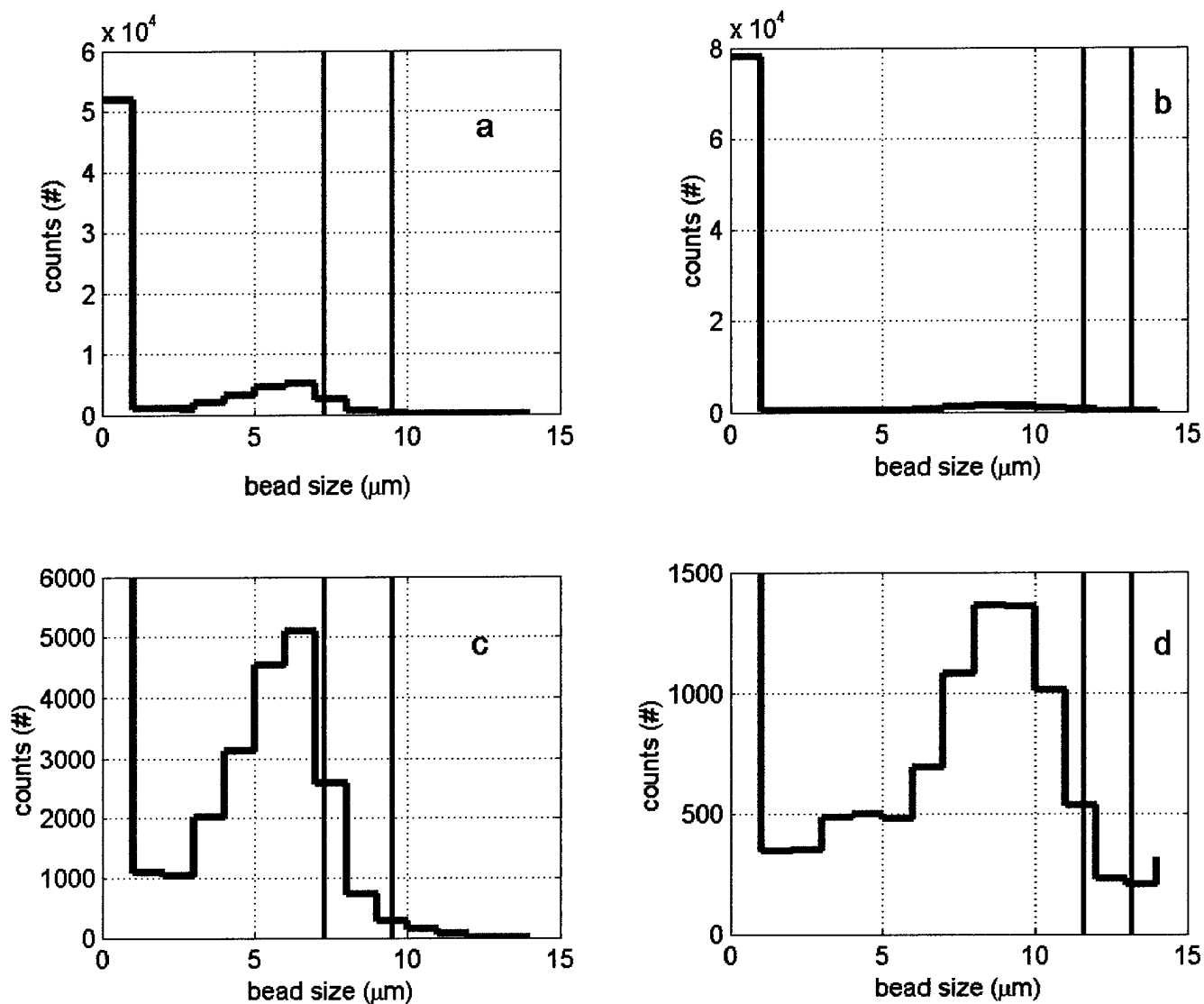


**Figure 29.** Bead size distributions measured by the FSSP on Range 2, with the calibration insert and aspiration tube. The nominal bead diameter for each histogram is a.) 10 μm, b.) 14.5 μm, c.) 10 μm expanded scale, and d.) 14.5 μm expanded scale.

Figure 28 contains plots of histograms recorded with the inlet device present. In this size range, introducing the windows into the sample volume seemed to produce even more noise in the smallest size bin. These counts were present even when particles were not being introduced to the FSSP. A possible explanation for the high number of counts in the lowest size bin is contamination being present on the windows. Translating the inlet tube with the translation stage would change the number of counts, indicating that the position of the windows with respect to the detectors influenced the signal. If tiny particles scattering light on the window surfaces are the cause of this erroneous signal, moving the particles should change the amount of light reaching the detectors. In order to be interpreted as a particle, the signal detector and annular detector must receive the appropriate light levels to determine the particle is within the depth of field. At the center of the depth of field the signal on the signal detector is maximum while the signal on the annular detector is minimum. As a particle moves out of the depth of field, the signal on the annular detector increases and it eventually reaches a level that is declared to be out of the depth of field. The locations of the window surfaces are clearly out of the depth of field and particles on these surfaces should be scattering sufficient light onto the annular detector to be rejected. However, the high sensitivity to noise in the smallest size bin when the FSSP is set on range 2 precludes a rigorous quantitative interpretation of the results.

Figures 28c and 28d have the scale on the y-axis expanded to indicate many particles are being recorded in the other size bins. The counts in these bins are much higher than in Figure 27c and 27d because of the improved targeting. The peak number of counts appears in relatively the same bins as in Figure 27c and 27d, just smaller than the expected equivalent water drop diameter.

Figure 29 presents data collected in experimental configuration three. Again, there is a lot of noise in the lowest size bin. Figures 29c and 29d show histograms that look very similar to those in Figure 28c and 28d, indicating the FSSP is sizing the particles in the same size bins as the other two experimental configurations.

### 3.4.5 Discussion of Laboratory Results

Table VI lists the median diameter and mode diameter for each of the histograms presented. In the case of Figures 27, 28, and 29, the lowest two size bins have not been included in the mean and median calculation because they would severely bias the calculation and not accurately represent the measured values of the glass beads.

The results in Table VI show that the inlet calibration device does not alter the response of the FSSP-100. In particular, the values of the size mode (i.e., the channel that contains the most counts), shown in Table VI by the yellow columns, is nearly unaffected by the insertion of the inlet calibration device. The mode was the same throughout all of the runs except for a one-bin shift using the 14.5  $\mu\text{m}$  beads in range 0

and range 2. In these cases, the one-bin shift occurred once with the exit tube inserted and once without the exit tube, suggesting that it may be a random event.

	Range 0						Range 1						Range 2					
	FSSP w/o Inlet Installed		FSSP with Inlet		FSSP with Inlet & Tube		FSSP w/o Inlet Installed		FSSP with Inlet		FSSP with Inlet & Tube		FSSP w/o Inlet Installed		FSSP with Inlet		FSSP with Inlet & Tube	
Bead Dia( $\mu$ m)	Mean ( $\mu$ m)	Mode ( $\mu$ m)	Mean ( $\mu$ m)	Mode ( $\mu$ m)	Mean ( $\mu$ m)	Mode ( $\mu$ m)	Mean ( $\mu$ m)	Mode ( $\mu$ m)	Mean ( $\mu$ m)	Mode ( $\mu$ m)	Mean ( $\mu$ m)	Mode ( $\mu$ m)	Mean ( $\mu$ m)	Mode ( $\mu$ m)	Mean ( $\mu$ m)	Mode ( $\mu$ m)	Mean ( $\mu$ m)	Mode ( $\mu$ m)
10	6.5	6.5	7.4	6.5	6.7	6.5	7.2	7	7.7	7	7.4	7	6.9	7.5	7.1	7.5	6.7	7.5
14.5	10.1	9.5	11.2	12.5	10.3	9.5	10.6	11	11.3	11	11.1	11	10.2	10.5	9.6	10.5	9.3	9.5
20	13.9	15.5	16.4	15.5	15.6	15.5	13.9	17	16.1	17	15.8	17	-	-	-	-	-	-
40	12.7	27.5	22.4	27.5	24.1	27.5	-	-	-	-	-	-	-	-	-	-	-	-

**Table VI.** Mean and Mode diameter for each experimental configuration in each size range.

Also, with the exception of the 40  $\mu$ m bead case, the mean diameters for all experimental configurations in all size ranges agree very well. When comparing experimental configurations without the inlet calibration device and with the calibration device and tube inserted, the mean diameter is within one bin width or less for all cases except that of 40  $\mu$ m beads. The mode diameter is relatively insensitive to potential problems with the depth of field rejection compared to the mean diameter. Due to the depth of field consideration, the targeting of the particles may bias the calculation of the mean diameter more than it affects the mode diameter. Mode diameter may be the best indicator of bead sizing and the effect of the calibration inlet device on the bead sizing.

## 4. Conclusions and Recommendations for Phase II

In all experimental configurations for the expected equivalent water drop diameter, the SPEC FSSP-100 sized most of the beads in the appropriate size bin, or one size bin smaller. For size ranges zero and one, the effect of the inlet calibration device was negligible, as predicted by the optical simulations. For size range two, noise or contamination on the windows of the inlet calibration device may have created false particle counts in the lowest size bin. However, on range 2, the FSSP still sized the

particles correctly in the other bins of this size range. Thus, the laboratory tests show that the inlet calibration device satisfies the two requirements for successful application on a research aircraft:

- i.* The inlet calibration device was successfully fabricated with smooth cylindrical interior walls so that the airflow velocity distribution can be predicted from simple theory of flow through a pipe.
- ii.* The thin sapphire optical flats do not measurably degrade the sizing of the FSSP-100.

The proof-of-concept laboratory tests conducted in Phase I provide a strong foundation for adaptation of the inlet calibration device to a research aircraft in Phase II. We recommend that the following tasks be undertaken in Phase II.

1. Modify the laboratory version of the aerosol inlet calibration device designed in Phase I for application on a research aircraft. Build two inlet calibration devices (one for flight tests with the SPEC Learjet and another for the Navy Twin Otter) and perform additional laboratory experiments with an FSSP-300.
2. Install a standard diffuser aerosol inlet on the SPEC Learjet.
3. Design and fabricate a new airborne dual-imaging probe for measuring particles from about 5 to 1000  $\mu\text{m}$  in size.
4. Equip the SPEC Learjet with an FSSP and the new dual-imaging probe installed in the wingtips, and an FSSP with the aerosol inlet calibration device installed in the cabin.
5. Evaluate the performance of the aerosol inlet calibration device by flying the specially equipped Learjet in atmospheres laden with large aerosols.
6. Analyze the data collected by the Learjet research aircraft and write the final Phase II report.

## **References**

- Albrecht, B.A., 1989: Science **245**, 1227.
- Ångström, A., 1929: On the atmospheric transmission of sun radiation and on dust in the air. *Geografiska Annaler*, **11**, 156-169.
- Baumgardner, D. and S. Skinner, 1989: Forward Scattering Spectrometer Probe (FSSP) Calibration and Maintenance Procedures Manual, Research Aviation Facility, NCAR, Boulder, CO 80307.

- Baumgardner, D., B. Huebert and J.C. Wilson (eds.), July, 1991: *Meeting Review: Airborne Aerosol Inlet Workshop, NCAR Tech. Note TN-362+1A*, 288 pp., Nat'l Cent. For Atmos. Res., Boulder, CO.
- Baumgardner, D., J. E. Dye, R. G. Knollenberg and B. W. Gandrud, 1992: Interpretation of measurements made by the FSSP-300X during the Airborne Arctic Stratospheric Expedition. *J. Geophys. Res.*, **97**, 8035-8046.
- Blomquist, B. W., B. J. Huebert, S. G. Howell, M. Litchy, C. Twohy, D. Baumgardner, B. Lafleur, R. Seebaugh and M. Laucks, 2000: An evaluation of the Community Aerosol Inlet for the NCAR C-130 Research Aircraft. *J. Atmos. Ocean. Technol.*, **18**, (8), 1387-1397.
- Boucher, O. and T. L. Anderson, 1995: General circulation model assessment of the sensitivity of direct climate forcing by anthropogenic sulfate aerosols to aerosol size and chemistry. *J. Geophys. Res.*, **100**(D12), 26,117-26,134.
- Charlson, R. J., W. M. Porch, A. P. Waggoner and N. C. Ahlquist, 1974: Background aerosol light scattering characteristics: Nephelometric observations at Mauna Loa Observatory compared with the results at other remote locations. *Tellus*, **26**, 345-360.
- Charlson, R. J., J. E. Lovelock, M. O. Andreae, and S. G. Warren, 1987: Oceanic phytoplankton, atmospheric sulphur, cloud albedo and climate. *Nature*, **326**, 655-661.
- Charlson, R. J., J. Langner, and H. Rodhe, 1990: Sulphate aerosol and climate. *Nature*, **348**, 22.
- Charlson, R. J., J. Langner, H. Rodhe, C. B. Leovy, and S. G. Warren, 1991: Perturbation of the northern hemisphere radiative balance by backscattering from anthropogenic sulfate aerosols. *Tellus*, **43AB**, 152-163.
- Charlson, R. J., S. E. Schwartz, J. M. Hales, R. D. Cess, J. A. Coakley, Jr., J. E. Hansen and D.J. Hoffmann, 1992: Climate Forcing by Anthropogenic Aerosols. *Science*, **255**, 423-430.
- Dye, J.E. and D. Baumgardner, 1984: Evaluation of the forward scattering spectrometer probe: Part I. Electronic and optical studies. *J. Atmos. Oceanic Technol.* **1**, 329-344.
- Hegg, D. A., L. F. Radke, and P. V. Hobbs, 1991: Measurements of Aitken Nuclei and Cloud Condensation Nuclei in the Marine Atmosphere and Their Relation to the DMS-Cloud-Climate Hypothesis, *Journal of Geophysical Research*, **96**, No. D10, 18,727-18,733.
- Hobbs, P. V., H. Harrison, and E. Robinson, 1974: Atmospheric effects of pollutants. *Science*, **183**, 909-915.
- Huebert, B. J., G. Lee and W. L. Warren, 1990: Airborne aerosol inlet efficiency measurement. *J. Geophys. Res.*, **95**(D10), 16,369-16,381.
- Huebert, B. J., S. G. Howell, D. Covert, A. Clarke and J. R. Anderson, 2000: Passing Efficiency of a Low Turbulence Inlet. *Final Report to NSF*. Available at <http://saga.pmel.noaa.gov/aceasia/>.
- Laird, N. F., H. T. Ochs III, R. M. Rauber and L. J. Miller, 2000: Initial Precipitation Formation in Warm Florida Cumulus. *J. Atmos. Sciences*. **57**, 3740-3751.

- Mitchell, J. M., 1975: *The Changing Global Climate*, Reidel, Dordrecht, S. F. Singer, ed., 149-173.
- Nemesure, S., R. Wagener and S. E. Schwartz, 1995: Direct shortwave forcing of climate by the anthropogenic sulfate aerosol: Sensitivity to particle size, composition, and relative humidity. *J. Geophys. Res.*, **100**(D12), 26,105-26,116.
- Porter, J. N., A. D. Clarke, G. Ferry and R. F. Pueschel, 1992: Aircraft studies of size-dependent aerosol sampling through inlets. *J. Geophys. Res.*, **97**(D4), 3815-3824.
- Rosenfeld, D., 1999: *Geophys. Res. Letters*, **26**, 3105
- Rosenfeld, D., 2000: Suppression of Rain and Snow by Urban and Industrial Air Pollution. *Science*, **287**, 1793-1796.
- Seebaugh, W. R., B. G. Lafleur, J. C. Wilson and J. Kim, 1997: Low Turbulence Inlet for Airborne Aerosol Sampling. Patent Disclosure to the University of Denver.
- Sheridan, P. J. and R. B. Norton, 1998: Determination of the passing efficiency for aerosol chemical species through a typical aircraft-mounted, diffuser-type aerosol inlet system. *J. Geophys. Res.*, **103**(D7), 8215-8225.
- Tanner, R. L., R. Cederwall, R. Garber, D. Leahy, W. Marlow, R. Meyers, M. Phillips, and L. Newman, 1977: Separation and analysis of aerosol sulfate species at ambient concentrations. *Atmos. Environ.*, **11**, 955.
- Tegen, I., A. A. Lacis and I. Fung, 1996: The influence on climate forcing of mineral aerosols from disturbed soils. *Nature*, **380**, 419-422.
- Tennekes, H. and J. L. Lumley, 1972: *A First Course in Turbulence*. The Massachusetts Institute of Technology Press, Cambridge, MA. 300 pp.
- Twomey, S. A., M. Peipgrass, and T. L. Wolfe, 1984: An assessment of the impact of pollution on global cloud albedo. *Tellus*, **36B**, 356-366.
- Wigley, T. M. L., 1989: Possible climate change due to SO<sup>2</sup> derived cloud condensation nuclei. *Nature*, **339**, 365-367.
- Wigley, T. M. L., 1991: Could reducing fossil-fuel emissions cause global warming? *Nature*, **349**, 503-506.